



HAL
open science

Dark Galaxy Candidates at Redshift ~ 3.5 Detected with MUSE

Raffaella Anna Marino, Sebastiano Cantalupo, Simon J Lilly, Sofia G Gallego, Lorrie A Straka, Elena Borisova, Gabriele Pezzulli, Roland Bacon, Jarle Brinchmann, C. Marcella Marcella Carollo, et al.

► **To cite this version:**

Raffaella Anna Marino, Sebastiano Cantalupo, Simon J Lilly, Sofia G Gallego, Lorrie A Straka, et al.. Dark Galaxy Candidates at Redshift ~ 3.5 Detected with MUSE. *The Astrophysical Journal*, 2018, 859 (1), pp.53. 10.3847/1538-4357/aab6aa . hal-02325340

HAL Id: hal-02325340

<https://hal.science/hal-02325340v1>

Submitted on 22 Oct 2019

HAL is a multi-disciplinary open access archive for the deposit and dissemination of scientific research documents, whether they are published or not. The documents may come from teaching and research institutions in France or abroad, or from public or private research centers.

L'archive ouverte pluridisciplinaire **HAL**, est destinée au dépôt et à la diffusion de documents scientifiques de niveau recherche, publiés ou non, émanant des établissements d'enseignement et de recherche français ou étrangers, des laboratoires publics ou privés.



Distributed under a Creative Commons Attribution 4.0 International License



Dark Galaxy Candidates at Redshift ~ 3.5 Detected with MUSE*

Raffaella Anna Marino¹, Sebastiano Cantalupo¹, Simon J. Lilly¹, Sofia G. Gallego¹, Lorrie A. Straka², Elena Borisova³, Gabriele Pezzulli¹, Roland Bacon⁴, Jarle Brinchmann^{2,5}, C. Marcella Carollo¹, Joseph Caruana^{6,7}, Simon Conseil⁴, Thierry Contini⁸, Catrina Diener⁹, Hayley Finley^{8,10}, Hanae Inami⁴, Floriane Leclercq⁴, Sowgat Muzahid², Johan Richard⁴, Joop Schaye², Martin Wendt^{11,12}, and Lutz Wisotzki¹²

¹ Department of Physics, ETH Zürich, Wolfgang—Pauli—Strasse 27, 8093 Zürich, Switzerland; marinor@phys.ethz.ch

² Leiden Observatory, Leiden University, P.O. Box 9513, 2300 RA Leiden, The Netherlands

³ Paul Scherrer Institute, WBB/214, 5232 Villigen PSI, Switzerland

⁴ Université Lyon 1, Ens de Lyon, CNRS, Centre de Recherche Astrophysique de Lyon UMR5574, F-69230, Saint-Genis-Laval, France

⁵ Instituto de Astrofísica e Ciências do Espaço, Universidade do Porto, CAUP, Rua das Estrelas, PT4150-762 Porto, Portugal

⁶ Department of Physics, University of Malta, Msida MSD 2080, Malta

⁷ Institute for Space Sciences and Astronomy, University of Malta, Msida MSD 2080, Malta

⁸ Institut de Recherche en Astrophysique et Planétologie (IRAP), Université de Toulouse, CNRS, UPS, F-31400 Toulouse, France

⁹ Institute of Astronomy, Madingley Road Cambridge, CB3 0HA, UK

¹⁰ Université de Toulouse, UPS-OMP, F-31400 Toulouse, France

¹¹ Institut für Physik und Astronomie, Universität Potsdam, Karl-Liebknecht-Str. 24/25, D-14476 Golm, Germany

¹² Leibniz-Institut für Astrophysik Potsdam (AIP), An der Sternwarte 16, D-14482 Potsdam, Germany

Received 2017 September 8; revised 2018 March 9; accepted 2018 March 12; published 2018 May 23

Abstract

Recent theoretical models suggest that the early phase of galaxy formation could involve an epoch when galaxies are gas rich but inefficient at forming stars: a “dark galaxy” phase. Here, we report the results of our Multi-Unit Spectroscopic Explorer (MUSE) survey for dark galaxies fluorescently illuminated by quasars at $z > 3$. Compared to previous studies which are based on deep narrowband (NB) imaging, our integral field survey provides a nearly uniform sensitivity coverage over a large volume in redshift space around the quasars as well as full spectral information at each location. Thanks to these unique features, we are able to build control samples at large redshift distances from the quasars using the same data taken under the same conditions. By comparing the rest-frame equivalent width (EW_0) distributions of the $Ly\alpha$ sources detected in proximity to the quasars and in control samples, we detect a clear correlation between the locations of high- EW_0 objects and the quasars. This correlation is not seen in other properties, such as $Ly\alpha$ luminosities or volume overdensities, suggesting the possible fluorescent nature of at least some of these objects. Among these, we find six sources without continuum counterparts and EW_0 limits larger than 240 Å that are the best candidates for dark galaxies in our survey at $z > 3.5$. The volume densities and properties, including inferred gas masses and star formation efficiencies, of these dark galaxy candidates are similar to those of previously detected candidates at $z \approx 2.4$ in NB surveys. Moreover, if the most distant of these are fluorescently illuminated by the quasar, our results also provide a lower limit of $t = 60$ Myr on the quasar lifetime.

Key words: galaxies: formation – galaxies: high-redshift – galaxies: star formation – intergalactic medium – quasars: emission lines – quasars: general

Supporting material: machine-readable table

1. Introduction

Despite a great deal of progress in defining the demographics of galaxies at high redshift ($z > 3$), our knowledge about the fuel for the formation of the first stars, i.e., the cold gas ($T \leq 10^4$ K) surrounding the galaxies, is still limited. In addition, due to small sample sizes and technical limitations of the current facilities (Fumagalli et al. 2014), how this gas forms the large-scale structure of the universe, the intergalactic medium (IGM), and how it fuels active star formation (SF) over time are unclear processes (Cantalupo et al. 2012, hereafter C12).

* Based on observations obtained at the Very Large Telescope (VLT) of the European Southern Observatory, Paranal, Chile (ESO Programme IDs 094.A-0396, 095.A-0708, 096.A-0345, 097.A-0251, 098.A-0678, 094.A-0131, 095.A-0200, 096.A-0222, 097.A-0089, 098.A-0216).

It has been established that the densest and most filamentary parts of the IGM play a key role in the formation and evolution of galaxies (Meiksin 2009 and references therein). Recent observations have raised our awareness of the nature of the IGM and CGM (circumgalactic medium), thanks to both the absorption (Giavalisco et al. 2011; Turner et al. 2014) and emission (e.g., Borisova et al. 2016b; Wisotzki et al. 2016) signatures of hydrogen at several scales and in different environments, from quasars (QSOs) to radio galaxies (e.g., Cantalupo et al. 2014; Swinbank et al. 2015; Cantalupo 2017).

Theoretical models have suggested the existence of a primordial phase (which is almost optically dark) in galaxy formation where gas-rich galaxies reside in low-mass halos (e.g., Dekel et al. 2009; Krumholz & Dekel 2012; Kuhlen et al. 2012) with very low SF efficiencies ($SFEs = SFR/M_{\text{gas}} < 10^{-11} \text{ yr}^{-1}$). This less efficient SF phase of the IGM gas at high redshift could be due to the metal-free gas present in the environment at that epoch, to the H_2 self-regulation effect (Kuhlen et al. 2012), or even to a reduced CGM cooling rate (Cantalupo 2010).

Different approaches have been taken to further investigate this dark phase of galaxy formation in the literature. The different methods that have been used in the past to try to detect the “starless” IGM gas, i.e., just before considerable SF occurs, are:

- (i) *H I absorption systems* along the line of sight to bright background sources (QSOs) at high redshift (e.g., Fumagalli et al. 2011; Rudie et al. 2012; Prochaska et al. 2013a, 2013b; Lee et al. 2014; Johnson et al. 2015; Lau et al. 2016, among others) using one-dimensional data. This method cannot help in discerning between real isolated dark clouds or gas reservoirs within/around galaxies without the additional information on spatial extent that comes from the emission of the neutral gas.
- (ii) *H I 21 cm direct imaging* (e.g., Giovanelli et al. 2005; Gavazzi et al. 2008). This approach is observationally limited to the dark clouds detected in the local universe because this line is too weak to be detected at high redshift using current ground-based telescopes.
- (iii) *Fluorescent emission induced by the cosmic ultraviolet background (UVB)*, as proposed by the pioneering works of Hogan & Weymann (1987) and Gould & Weinberg (1996). This radiation is produced by ionized gas that recombines and emits fluorescent H I Ly α ¹³ photons (Cantalupo et al. 2005). The main drawback of this method is the intrinsic faintness of the UVB emission that would imply an Ly α surface brightness (SB) of $SB \sim 10^{-20} \text{ erg s}^{-1} \text{ cm}^{-2} \text{ arcsec}^{-2}$ (Rauch et al. 2008), which makes detection with current facilities very challenging.
- (iv) *QSO-induced fluorescent Ly α emission* can locally boost the signal from dense and otherwise dark gas clouds by orders of magnitude (Haiman & Rees 2001; Cantalupo et al. 2005; Kollmeier et al. 2010; Martin et al. 2014; C12), acting as a flashlight on its surroundings. Notwithstanding the complex interpretation of the physics behind the Ly α fluorescence (e.g., Fynbo et al. 2003; Francis & Bland-Hawthorn 2004; Cantalupo et al. 2007; Rauch et al. 2008; Hennawi & Prochaska 2013; Trainor & Steidel 2013, among others), thanks to the support of 3D radiative transfer models, this seems to be the most promising observational approach and forms the basis of the present investigation using MUSE (Multi-Unit Spectroscopic Explorer).

Our approach is based on the QSOs that photoionize the surrounding gas, boosting the faint Ly α fluorescent glow expected from the cold gas by a factor of 100–1000 (within a distance of about 10 comoving Mpc) with respect to fluorescence due to the UVB only. Uncertainties include the variable luminosities of the QSOs, the uncertain UV continuum (Lusso et al. 2015), the QSO opening angle (Trainor & Steidel 2013), and further complexities related to the resonant nature of the Ly α line.

Despite the predictions by several numerical simulations and observational efforts with 8–10 m class telescopes, in most of the studies conducted so far, the protogalactic phase preceding the first spark of SF has been poorly constrained. The most convincing observational evidence for this dark phase at high redshift are the objects presented in C12. Using the fluorescent emission induced by the QSO UM 287 at redshift 2.4, they

detected 12 dense and compact gas-rich emitters in a 20 hr-deep narrowband (NB) image with VLT-FORS. These emitters, named “Dark Galaxies” (DGs hereafter), have no detected continuum (stellar) counterpart. The rest-frame equivalent widths, $EW_0 > 240 \text{ \AA}$, of these DGs cannot be easily explained by normal star-forming regions (Salpeter stellar initial mass function (IMF); Charlot & Fall 1993; Malhotra & Rhoads 2002). There are several limitations in the methodology employed in C12. For instance, it requires a custom-made NB filter centered on the QSO redshift. This demands that (i) the estimation of the QSO redshift must be very precise, (ii) the results have to take into account possible filter losses, and (iii) the candidates need to be confirmed with spectroscopic data. Another limitation concerns the comparison of their results with previous works, because their control samples can be affected by the different observational strategies of the “blank-field” surveys in the literature.

Therefore, the challenging question that we would like to consider here regarding the nature of DGs is:

Do DGs exist at higher ($z > 2.4$) redshifts, and what can be learned from their redshift evolution?

In order to answer this question, we use an alternative approach to NB imaging to search for the fluorescent Ly α emission produced by bright QSOs at $z > 3$. Integral Field Units (IFUs), like the MUSE instrument (Bacon et al. 2010), offer an unparalleled opportunity for this kind of study. MUSE has several advantages over previous instrumental techniques: homogeneous data quality, large wavelength range (which translate into a large cosmological volume), and bidimensional information for robust analysis. Such strengths enable the final aim of this study to investigate how the IGM gas is converted into stars.

With the help of the third dimension, i.e., the wavelength information missing from NB surveys, we have direct spectroscopic confirmation and also the possibility to explore the presence of other emission lines (e.g., [C IV] $\lambda\lambda 1548, 1550$ and [He II] $\lambda 1640$). More importantly, the use of Integral Field Spectroscopy (IFS) provides the ability to build control samples with essentially the same instrumental and observational conditions, as well as data reduction and analysis techniques, with respect to the main data set. One drawback is the relatively small MUSE field of view (MUSE FoV $1' \times 1'$) with respect to the previous NB images of C12 (VLT-FORS FoV $\sim 7' \times 7'$) in exploring the fluorescent volume around the QSO. Indeed, based on the C12 work, we expect to find only one or two DGs per MUSE field around each QSO. For this reason, in this paper we combine medium-deep MUSE observations (>9 hr total exposure time per field) obtained on six different fields containing bright QSOs.

Here, we present the MUSE detection of 11 high- EW_0 ($>240 \text{ \AA}$) objects within six medium-deep (>9 hr) fields at $z > 3$, of which eight of these intriguing objects are possible DG candidates fluorescently illuminated by the QSOs. In addition, we present the discovery of a (control sample) population of ~ 200 Ly α emitters (LAEs) detected in the same fields.

The paper is organized as follows. In Section 2, we describe the sample providing details of the MUSE observations, data reduction, and postprocessing. In Section 3, we present the systematic analysis of both continuum-detected and -undetected Ly α emitters within the six MUSE fields. Our results are presented in Section 4, and we discuss our findings in Section 5.

¹³ H I Ly α line = atomic hydrogen de-excitation from the 2^2P to the 1^2S level that results in the emission of a single photon with energy 10.2 eV and $\lambda = 1215.67 \text{ \AA}$.

The summary and conclusions are presented in Section 6. Finally, we publish the catalog of LAEs in Table 5.

Throughout the paper we adopt a flat Λ CDM cosmology with *Wilkinson Microwave Anisotropy Probe 9* (WMAP9) cosmological parameters of $\Omega_{\Lambda} = 0.714$, $\Omega_M = 0.286$, and $h = 0.693$ (Hinshaw et al. 2013), corresponding to ~ 7.5 kpc/arcsec at redshift ~ 3 . We use vacuum wavelengths for the spectral analysis, and all magnitudes are in units of the AB system (Oke & Gunn 1983).

2. Sample and Observations

Our observations were carried out with MUSE, the second-generation IFU mounted on the Very Large Telescope (VLT) at the Nasmyth B focus of the Yepun (Unit Telescope 4) in Paranal, Chile. MUSE has a uniquely powerful performance: a relatively large FoV¹⁴ (in wide-field mode, WFM, $1' \times 1'$) combined with the excellent spatial sampling ($0''.2$) and spectral resolutions (R from ~ 1750 to ~ 3500) over a wide optical wavelength window (from 4650 to 9300 Å) and high throughput (35% at 7500 Å).

2.1. Sample

The six medium-deep fields at $z > 3$ analyzed in this study were observed between 2014 September and 2016 April. They form part of two MUSE Guaranteed Time Observation (GTO) programs (094.A-0396, 095.A-0708, 096.A-0345, 097.A-0251, 098.A-0678 PI: S. Lilly; 094.A-0131, 095.A-0200, 096.A-0222, 097.A-0089, 098.A-0216; PI: J. Schaye). The observations comprise 270 exposures (≈ 65 hr) in total. Each MUSE datacube consists of 321×328 spaxels with a sampling grid of $0''.2 \times 0''.2 \times 1.25$ Å, yielding $\sim 90,000$ spectra per frame. We use SExtractor (Bertin & Arnouts 1996) and QFitsView¹⁵ on the NB images centered at 7000 Å to measure the seeing (mean FWHM) on the final combined datacubes. We perform a Gaussian fit to the brightest point sources in each frame. From this, we obtain an average seeing across all frames better than $0''.85$. Most of the observations were carried out under clear or photometric conditions. From the quality assessment of the final combined MUSE datacubes, we obtain a mean (over the six fields) 3σ flux continuum limit in a $1''$ diameter aperture of 28.5 AB mag, whereas 30.5 AB mag represents the mean sensitivity value for the Ly α flux detection (see Section 3.4 for details on how these sensitivities were computed). Table 1 summarizes the measured properties for each field. Their short individual descriptions are provided in the next section. The composite pseudo-color images constructed from the MUSE datacube combining the broad V-, R-, and I-band images are shown in Figures 1 and 2. We decided to split our sample into two subsamples using the redshifts of the targeted QSOs in the respective fields, since our observations target six fields with a difference in the QSO redshift of $\Delta z \approx 0.7$ (maximum). Such a difference can be important in terms of both cosmological surface brightness dimming (Tolman 1930, 1934), which scales as $(1+z)^4$, as well as in

terms of the explored physical volume. Throughout this paper, we will use the term “lower-redshift sample” to refer to the fields at $z < 3.2$ and “high-redshift sample” to refer to those at $z > 3.7$.

2.1.1. Notes on Individual Fields

2.1.1.1. Low-redshift Sample

Q0422–3837 or Bulb Nebula: This is the lowest-redshift field, $z = 3.094$, within our sample. Different from the other fields in our sample, this observation targeted a known Ly α nebula around a galaxy that is ~ 19 comoving Mpc (cMpc) from a bright QSO. It was discovered through NB imaging (Borisova et al. 2016a). Our MUSE observations revealed a previously unknown Type II active galactic nucleus (AGN) at its center, $\alpha_{(J2000)} = 04:22:01.5$ and $\delta_{(J2000)} = -38:37:19$. It was observed for 20 hr with MUSE. The size of the point-spread function (PSF) measured on the final datacube at 7000 Å and based on different point sources is $0''.7$ (the best seeing in our sample). This field is present in both the *GALEX* (Seibert et al. 2012) and *Spitzer* (Capak et al. 2012) catalogs, but to our knowledge nothing remarkable about this field has been previously published. The name Bulb comes from the appearance of the Ly α nebula around this AGN in the NB survey, which will be presented in a forthcoming paper (S. Cantalupo et al. 2018, in preparation). The RGB synthetic image is shown in the left panel of Figure 1, where the position of the AGN is marked with the red cross.

Q2321+0135 or Hammerhead Nebula: The second field in our low-redshift sample is centered on a radio-quiet (RQ)¹⁶ QSO at $z = 3.199$, $\alpha_{(J2000)} = 23:21:14.7$, and $\delta_{(J2000)} = +01:35:54$, and is presented in the right panel of Figure 1. This QSO was first spectroscopically discovered in Ly α emission by Schmidt et al. (1987) and was also observed in the Sloan Digital Sky Survey (SDSS; York et al. 2000) with a subsequent follow-up by the Baryon Oscillation Spectroscopic Survey (BOSS; Pâris et al. 2012). These authors confirmed the detection of the C IV λ 1550 line, which is likewise detected in the MUSE integrated spectra. The PSF measured at 7000 Å is $0''.76$. Similar to the Bulb case, a huge Ly α nebula around this QSO was discovered in NB imaging (Borisova 2016). More details on the Hammerhead will be provided in R. A. Marino et al. (2018, in preparation).

2.1.1.2. High-redshift Sample

Q0055–269: The RQ QSO Q0055–269, $\alpha_{(J2000)} = 00:57:58.1$ and $\delta_{(J2000)} = -26:43:14$, at $z = 3.662$ is part of our high-redshift sample. This interesting QSO presents several emission and absorption features also confirmed by previous UVES observations (Zafar et al. 2013), and it was the subject of many studies (Cimatti et al. 2002; Schaye et al. 2003; Boera et al. 2014, among others). The PSF measured on the 10 hr MUSE datacube is $0''.84$, and it was observed with a position angle (PA) of 70° as plotted in the top-left panel of Figure 2.

Q1317–0507: Q1317–0507 is an RQ QSO at $\alpha_{(J2000)} = 13:20:30.0$ and $\delta_{(J2000)} = -05:23:35$, at $z = 3.7$. Despite the poor photometric data available in the literature, this QSO has good spectral coverage with UVES. The original time exposure was

¹⁴ With respect to other FoV instruments, such as KMOS ($24 \times 2''.8 \times 2''.8$), NIRSpc ($3'' \times 3''$), PMAS-PPak ($74'' \times 64''$), SINFONI ($8'' \times 8''$), and VIMOS ($54'' \times 54''$), among others.

¹⁵ QFitsView v3.1 is a FITS file viewer using the QT widget library developed at the Max Planck Institute for Extraterrestrial Physics by Thomas Ott.

¹⁶ This classification is taken from the Véron-Cetty & Véron (2010) catalog and is based on the radio flux measured at 1.4 GHz, which for a RQ QSO should be < 5 mJy.

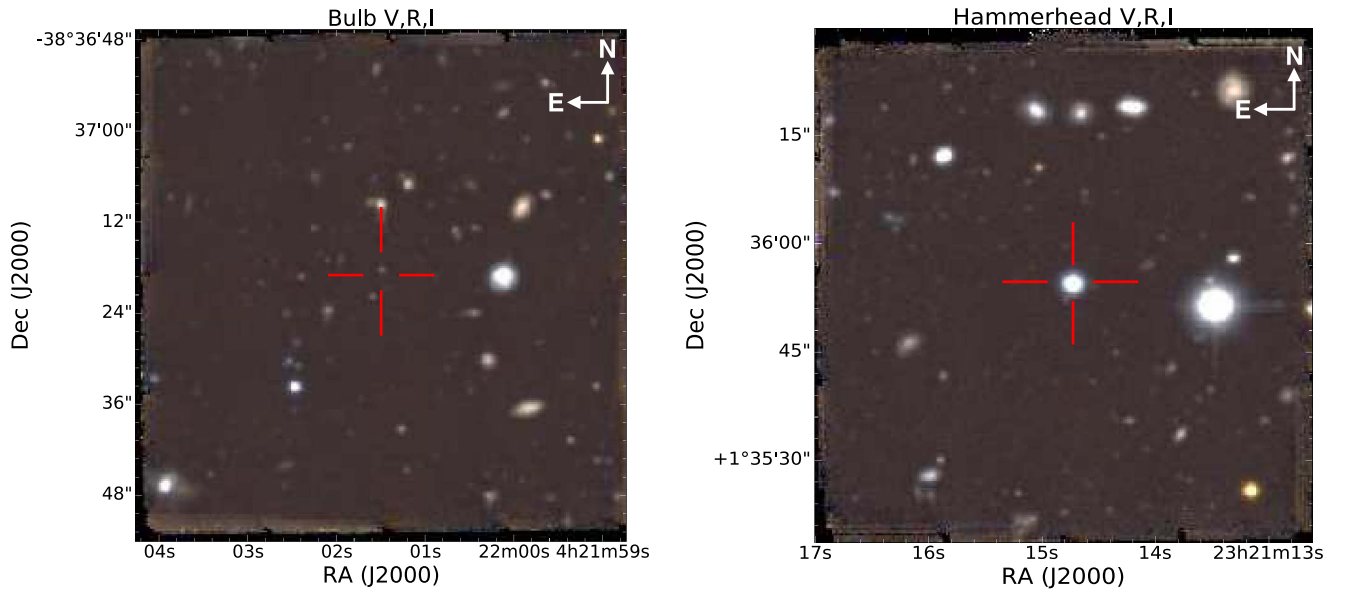


Figure 1. Composite pseudo-color images of the low-redshift ($z < 3.2$) MUSE fields. The RGB colors are assigned to V -, R -, and I -band images computed from the MUSE datacubes. Each image is $60'' \times 60''$, and the red cross indicates the AGN and QSO location in the case of the Bulb and Hammerhead fields, respectively.

Table 1
Major Properties of the MUSE Medium-deep Fields

	Bulb	Hammerhead	Q0055–269	Q1317–0507	Q1621–0042	Q2000–330
R.A. (J2000)	04:22:01.5	23:21:14.7	00:57:58.1	13:20:30.0	16:21:16.9	20:03:24.0
Decl. (J2000)	–38:37:19	+01:35:54	–26:43:14	–05:23:35	–00:42:50	–32:51:44
Redshift ^a	3.094	3.199	3.662	3.7	3.783	3.783
$z_{C\ IV}$ ^b	3.110	3.202	3.634	3.701	3.689	3.759
Exp. Time (hr)	20	9	10	9.75	8.75	10
Class ^c	Type II AGN	RQ QSO	RQ QSO	RQ QSO	RQ QSO	RL QSO
V^d (AB mag)	24.76	19.33	17.99	18.10	17.88	17.84
PSF ^e (arcsec)	0.70	0.76	0.84	0.74	0.77	0.84
$3\sigma_{Cont}$ @ $1''^f$ (AB mag)	29.0	28.4	28.6	28.3	28.2	28.5
$Ly\alpha$ Sensitivity @ $1''^f$ (AB mag)	30.8	30.2	30.5	30.6	30.3	30.7

Notes.

^a Redshift values from the catalog of Véron-Cetty & Véron (2010).

^b Computed from the luminosity-corrected (Shen et al. 2016) C IV emission-line measurement from the MUSE spectra.

^c Class refers to the type of powering source in the field, i.e., AGN, radio-quiet (RQ) QSO, and radio-loud (RL) QSO on the basis of the radio flux measurements (Flux [1.4 GHz] threshold 5 mJy) presented in the Véron-Cetty & Véron (2010) catalog.

^d Measured in a $3''$ diameter aperture on the reconstructed MUSE- V image, i.e., MUSE datacube convolved with the V -Johnson filter, without accounting for the foreground Galactic absorption.

^e Mean FWHM of the Gaussian fit measured on different point sources in the final combined datacube at 7000 \AA using both SExtractor and QFitsView tools.

^f These values are computed within a $1''$ diameter aperture.

10 hr but due to a satellite passing by during one observation, we simply rejected one exposure (15 minutes) to get a final combined integrated exposure time of 9.75 hr. The RGB image of this field is shown in the top-right panel of Figure 2, and the PSF measured is $0''.74$.

Q1621–0042: This RQ QSO, $\alpha_{(J2000)} = 16:21:16.9$ and $\delta_{(J2000)} = -00:42:50$, with $z = 3.7$, is part of the SDSS DR7 quasar catalog by Schneider et al. (2010). Due to the availability of panchromatic photometric observations together with UVES spectra, this is one of the metal-rich QSOs used to probe the time evolution of the C IV absorbers (Cooksey et al. 2013). The PSF for the 35 combined exposures (i.e., 8.75 hr; we had to exclude one problematic exposure due to its offset shifts) is $0''.77$.

Q2000–330: The highest-redshift field and the only radio-loud (RL) QSO within our sample is located at

$\alpha_{(J2000)} = 20:03:24.0$ and $\delta_{(J2000)} = -32:51:44$, with $z = 3.783$. The high-resolution spectrum of this QSO was taken with the Keck/HIRES (High Resolution Echelle Spectrometer; Vogt et al. 1994) instrument, and it is part of the Keck Observatory Database of Ionized Absorption toward Quasars (KODIAQ) survey (O’Meara et al. 2015) along with several other investigations mainly focused on characterizing the CGM. It was observed with MUSE for 10 hr with a PA of 30° . The PSF in the final datacube has a Gaussian FWHM of $0''.84$ at $\lambda = 7000 \text{ \AA}$.

2.2. Data Reduction and Postprocessing

The reduction of all 65 hr of MUSE data was performed using some of the standard recipes from the latest version of the ESO MUSE Data Reduction Software (DRS; pipeline version 1.6, Weilbacher 2015), complemented with the

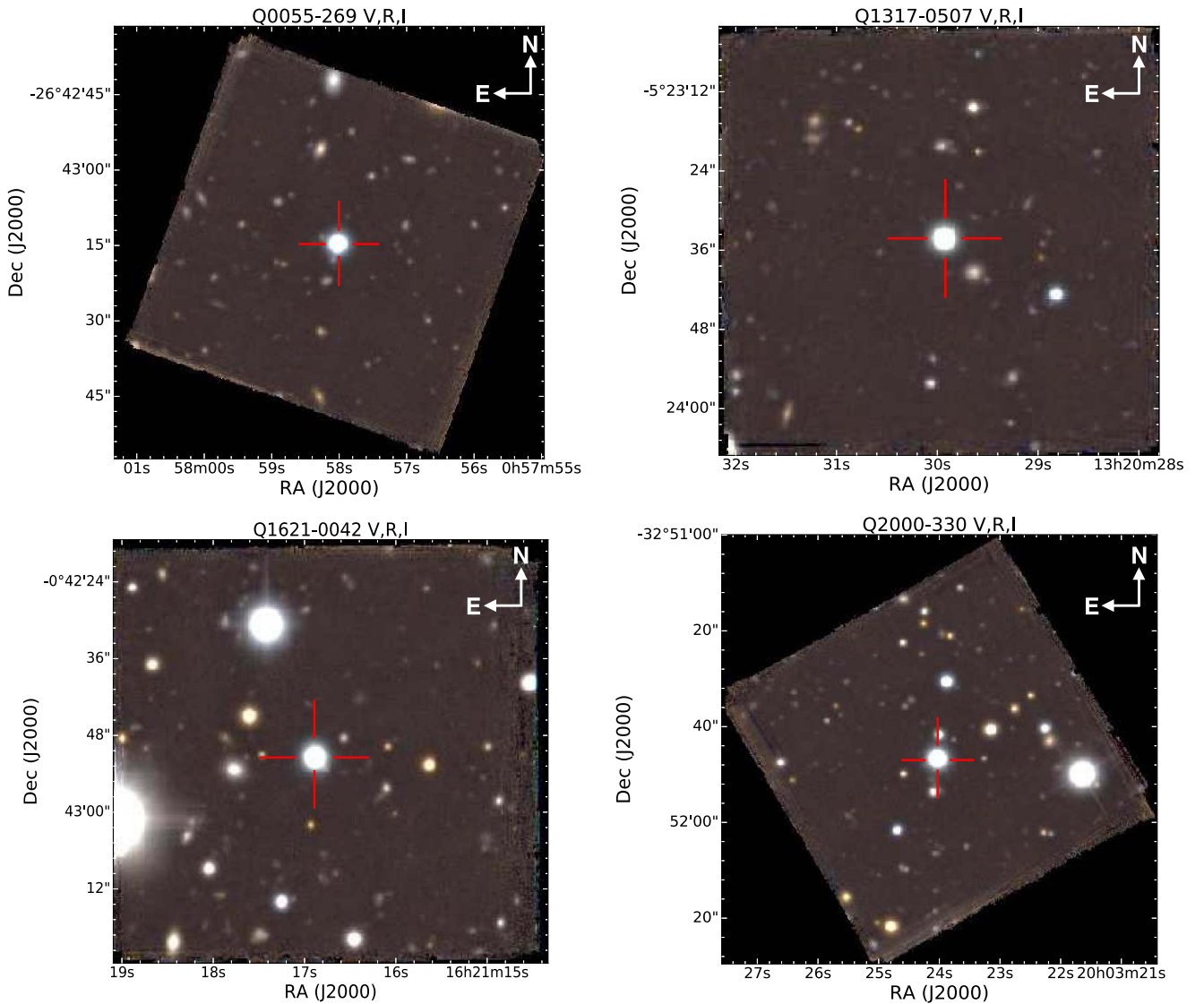


Figure 2. Composite pseudo-color images of the MUSE QSO fields at $z > 3.7$. The RGB colors are assigned to V -, R -, and I -band images from the MUSE datacubes. The red cross indicates the QSO location.

CubExtractor package (CubEx hereafter, version 1.6; S. Cantalupo 2018, in preparation), which was developed to optimize the flat-fielding correction and the sky-subtraction steps for our specific science case. After retrieving the raw data for each night, we first created the master calibration files using the MUSE pipeline, i.e., the master-bias, the master-flat, the twilight and illumination correction, and wavelength calibration files. Using the DRS routine MUSE scibasic, we processed each individual science exposure, both standard stars and QSO fields, applying the master calibration correction with the recommended parameters. For the illumination correction step, we always used the lamp flat-field and the twilight frames closest in time to each individual observation. All of these instrumental signatures are removed for each IFU (24 in total), and as output this recipe gives the pre-reduced pixel tables for every IFU exposure. Next, we use the MUSE scipost routine to create the individual datacubes by merging the pixel tables from all IFUs of each exposure. During this step, we also performed the flux calibration using the response curve and telluric absorption correction from one spectrophotometric standard observed during the same night. In addition, scipost

applies the geometry and astrometry tables available for each run to the science frames and performs a resampling (drizzle algorithm that maximizes the pixel fraction used) onto a 3D grid in order to construct the final datacube. Due to the fact that our observing strategy for each field included a $4 \times 90^{\circ}$ rotation pattern with small ($< 1''$) offsets (in order to minimize and smoothly distribute some residual structures, such as the ones observed at the edges of each slice stack), the automatic correction for the absolute astrometry obtained with the pipeline is a source of some uncertainty. For this reason, a double check of the pipeline astrometry correction was required, and in the case of clear residual offsets, we followed a more classic SExtractor approach in order to correct these offsets.

Once the pipeline-level datacubes were registered, we performed the postprocessing using the routines CubeFix, CubeAdd2Mask, CubeSharp, and CubeCombine within the CubEx package (S. Cantalupo 2018, in preparation), since we are interested in reaching very faint surface brightness levels. In particular, using CubeFix, we were able to remove the typical checkerboard pattern that is seen after the standard

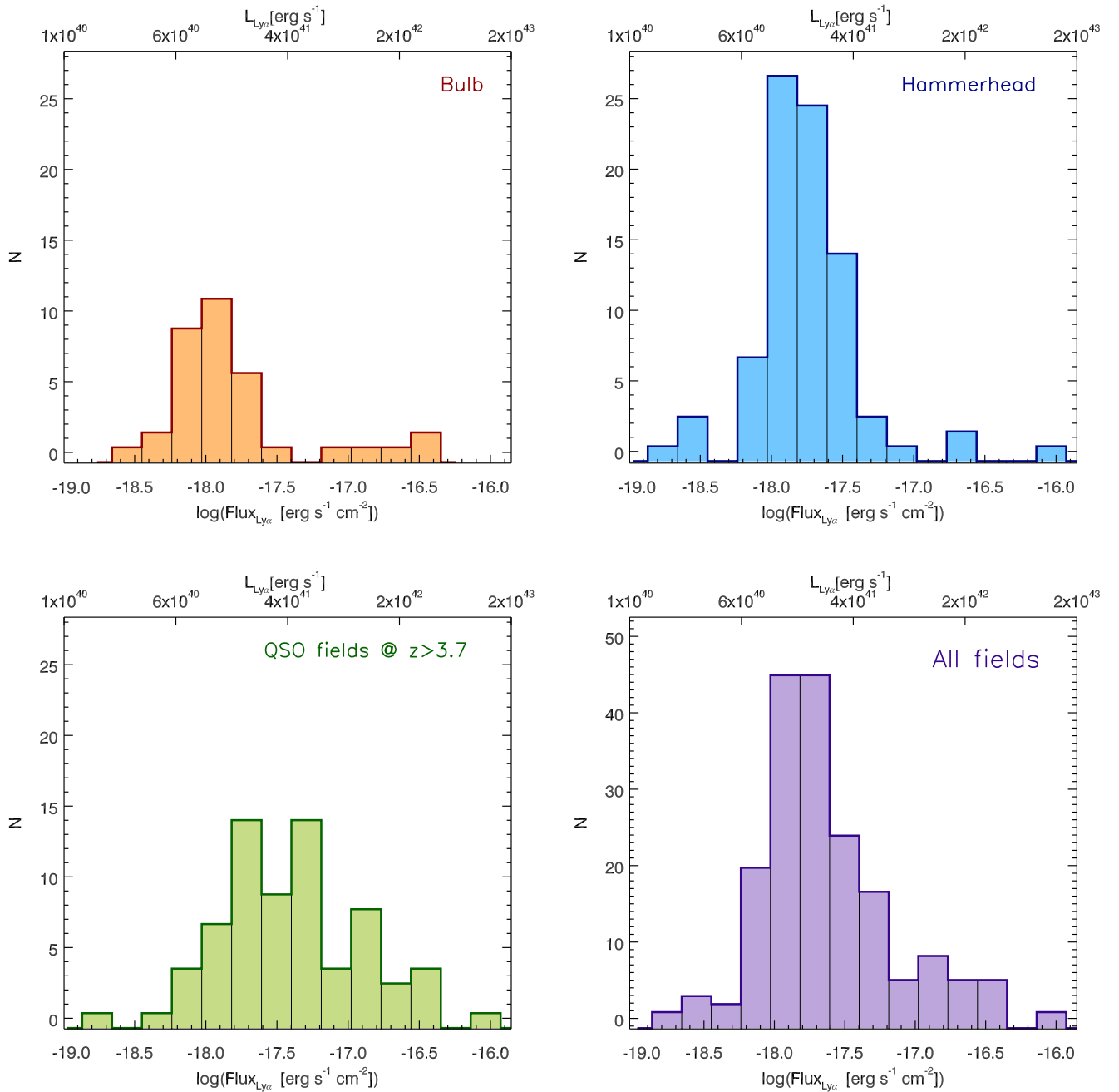


Figure 3. Ly α flux (and luminosity, top x -axis) distribution of all the LAEs detected within our MUSE medium-deep fields. In the top row, we plot the low-redshift sample, with the Bulb LAEs on the left and the Hammerhead ones on the right. The high-redshift sample is shown in the bottom-left panel. The distribution of all the detected LAEs is presented (with purple histograms) in the bottom-right panel.

data reduction with the pipeline. This is achieved because we self-calibrate each individual exposure at the level of the IFU, slice by slice, and vertical stacks using the sky continuum and the skylines as “flat sources” together with an iterative masking of any possible continuum sources. Thanks to the `CubeFix` flat-fielding correction, we were able to reduce the residuals to less than 0.1% of the sky level. Afterwards, we visually inspected the white-light (WL) images created from each `CubeFixed` datacube. In those cases where the edges of the individual IFU slices were still visible, or if there is a bright satellite trail or even a problematic channel, we performed manual masking using `CubeAdd2Mask`.

Then, we performed a local and flux-conserving sky subtraction on the `CubeFixed`–`CubeMasked` datacube using the `CubeSharp` routine. This empirical correction takes into account the skyline-spread function shifts and the variation across the MUSE FoV, conserving the flux and minimizing the residuals. Both `CubeFix` and `CubeSharp` were performed twice in order to minimize the contamination from possible unmasked sources when the illumination correction was applied.

Lastly, the `CubeFixed`–`CubeSharped` datacubes were combined with a 3σ clipping using both mean and median statistics with the `CubeCombine` routine. In the case of our analysis,

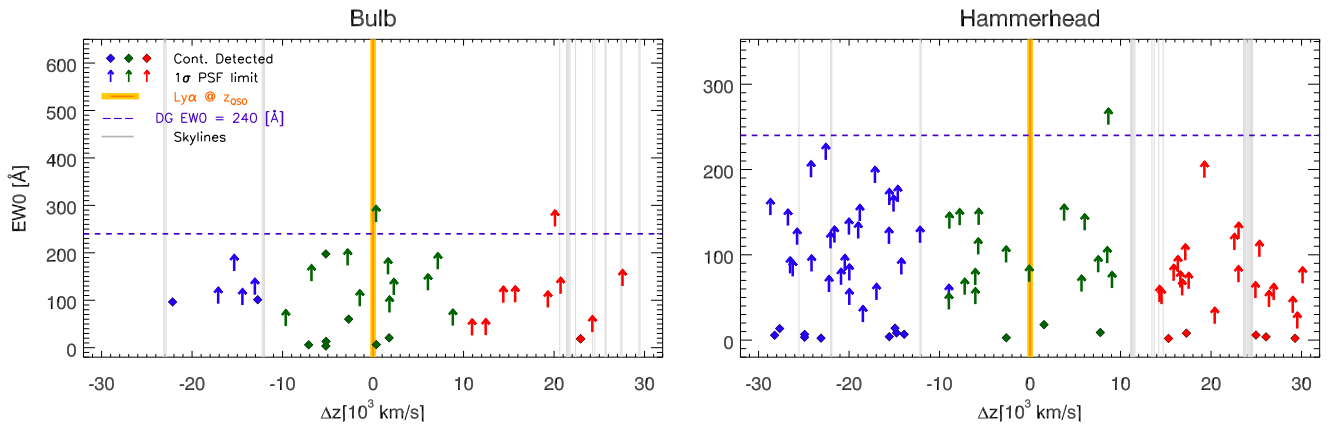


Figure 4. Rest-frame $\text{Ly}\alpha$ equivalent width (EW_0) values vs. the spectral distance (velocity) to the QSO of the detected $\text{Ly}\alpha$ emitters for the MUSE $z < 3.2$ sample. Blue and red symbols indicate those LAEs detected in the control samples, while green symbols show the LAEs closer to the QSO. Diamonds symbolize those LAEs with continuum counterparts, and the arrows show the lower limit (at 1σ) EW_0 values for continuum-undetected LAEs. The QSO velocity (plus the 1σ error) associated with the systemic redshift calibration (415 km s^{-1}) is marked with the shaded yellow area, and it was computed from the $\text{Ly}\alpha$ wavelength. The vertical gray shaded lines denote the masked OH skylines. The horizontal dashed line indicates the EW_0 threshold (240 \AA) for the DG candidates.

we use the mean-combined datacubes. We also refer the reader to Borisova et al. (2016b), Fumagalli et al. (2016, 2017), and North et al. (2017) for further details and additional applications of these reduction procedures.

3. Analysis

The goal of our analysis is to detect $\text{Ly}\alpha$ emitters within our sample. In this section, we describe our systematic search and classification of the $\text{Ly}\alpha$ emission candidates detected in the MUSE datacubes. In order to perform a consistent comparison between the six MUSE fields, we emphasize that the same methodology has been applied to all of the MUSE fields as detailed below.

3.1. PSF and Continuum Subtraction

Ideally, since we are interested in emission-line objects around the QSO (in both spectral and spatial directions) and not in QSO $\text{Ly}\alpha$ nebula, removing the nuclear contribution of the quasar should not be necessary for the detection of faint and compact targets. Nonetheless, we decided to perform a PSF subtraction to ensure minimum contamination from the QSO PSF in our LAE detection by making use of the empirical PSF subtraction of the `CubePSFSub` routine (part of the `CubeExtractor` package). Using an averaged-sigma-clipping algorithm, `CubePSFSub` constructs and rescales the QSO PSF using the NB images created for each wavelength layer, giving excellent results on large scales around the QSO (Borisova et al. 2016b). The next step was the subtraction of the brightest foreground continuum sources within our fields that were carefully removed using `CubeBKSub`. This routine estimates the continuum voxel by voxel¹⁷ on the basis of a median-filtering performed on the spectrum, which is integrated in 50 \AA bins and smoothed with a median filter radius of 3 pixels. This allows us to avoid any prominent line features and also to reduce the computational time. Some residuals are still visible in the output datacube, but this has a minimal impact on the extraction procedure of our LAEs considering that we are masking all of the bright continuum sources detected from the WL image.

¹⁷ The volumetric (3D spatial and spectral) pixel element in IFU datacubes.

3.2. Detection and Extraction of $\text{Ly}\alpha$ Emitters

One of the most important advantages of the IFS is that we can explore the same spatial area over a wide spectral range. To exploit the full capabilities of our MUSE data, our strategy to detect LAEs within our sample was to build three different subcubes from each datacube with the same spectral width of 200 \AA (or 160 spectral pixels). The on-source datacube is centered on the QSO $\text{Ly}\alpha$ wavelength. Two control sample subcubes adjacent to the on-source datacube were extracted on the blue and red sides. For practical reasons, they have the same spectral width as the on-source subcube. This choice of spectral width is justified in terms of the maximum volume (10 cMpc ; Trainor & Steidel 2013) where the signature of the fluorescent emission can be detected.

In total, we extracted six on-source datacubes. The LAEs observed in these samples are represented by green symbols in Figures 4, 5, and 7. We also extracted a total of 12 control sample datacubes, and the LAEs belonging to these sample are represented by blue and red colors in the same figures. As mentioned above, the difference in redshifts between our fields corresponds to slightly different analyzed volumes along the spectral direction, because of the constant area coverage. These distances span a range from 36 physical Mpc (pMpc) at redshift < 3.2 to 27 pMpc at redshift > 3.7 . We blindly implemented 3D source detection on the 18 reduced and postprocessed datacubes using `CubEx` with the same threshold parameters.

Aside from the routines described above, the main purpose of the `CubEx` software is the 3D automatic extraction of sources based on a novel approach used in computer science vision to detect connected regions in binary digital images (see S. Cantalupo 2018, in preparation). The algorithm uses subsets of connected components uniquely labeled on a user-defined property basis, e.g., connected-labeling-component (Shapiro & Stockman 2001). Specifically, we first smooth (with a radius of $0''.4$) both the science and variance datacubes only in the spatial directions for each wavelength layer. Then, we require that all detected objects fulfill three conditions: (i) a minimum of 40 connected voxels above a (ii) signal-to-noise ratio (S/N) threshold of 3.5 (after the re-scaling factor accounting for the propagated variance is applied) along with (iii) an S/N measured on the $\text{Ly}\alpha$ emission line from the 1D extracted spectrum above 4.5.

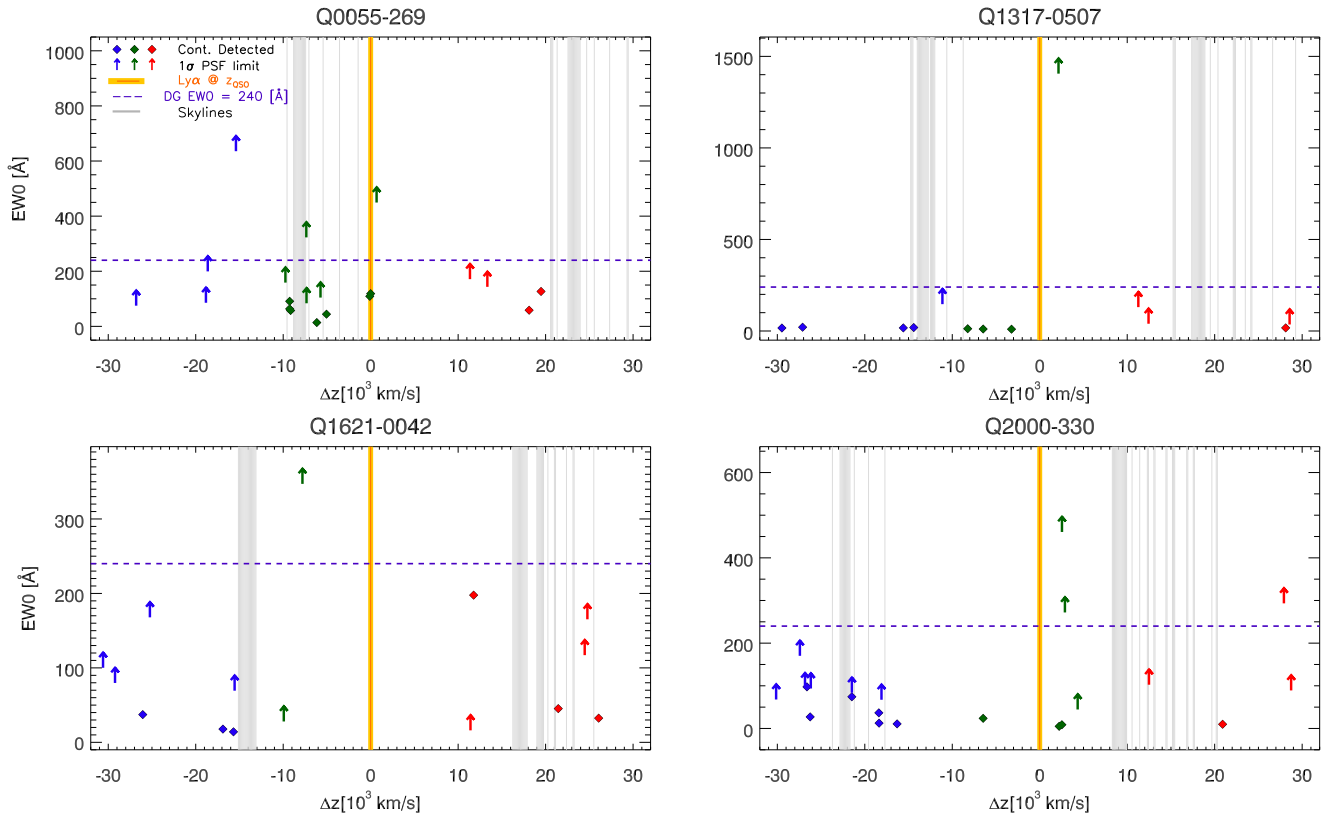


Figure 5. Rest-frame Ly α equivalent width (EW_0) values vs. the spectral distance (velocity) to the QSO of the detected Ly α emitters for the MUSE $z > 3.7$ sample. Symbols and colors are the same as for Figure 4.

Since the extraction process is based on the noise, estimating the noise correctly is a crucial ingredient of our selection criteria. Since the MUSE pipeline variance tends to be an underestimate of this noise (see Section 3 in Bacon et al. 2015), we use the propagated variance datacube computed by CubEx that takes the noise sources introduced by both the MUSE pipeline and the CubEx postprocessing steps into account. The propagated variance is used to calculate the re-scaling factor applied to each wavelength layer, which in the most extreme case is ≈ 1.95 . We also carefully mask the brightest and extended continuum sources detected in the WL image of each datacube,¹⁸ as well as possible skyline residuals to minimize possible artificial detections.

As a result of the 3D segmentation map, we obtain a full catalog of all the line emitters automatically detected in each MUSE field for the on-source and control sample datacubes.

3.3. Classification of the Ly α Emitters

Although we extensively tested our selection criteria, visual inspection is necessary to remove possible spurious detections of LAEs, such as possible contaminants from [O II] $\lambda\lambda 3726, 3729$, [O III] $\lambda 5007$, and AGN emitters that were able to pass through the previous masking. Therefore, for each object in our catalog, we tabulated both spectral and photometric information. Specifically, we visually checked the extracted 1D spectrum, where, accounting for different redshift solutions, we were able to

¹⁸ In order to select the brightest and extended continuum sources, we run CubEx on the datacubes using a detection threshold of $S/N = 10$. We also require each object to have a minimum of 100 connected voxels.

distinguish pure Ly α and other emitters by identifying the most prominent emission- and absorption-line features.

The results of our classification are summarized in Table 2, where we provide the full statistics of the detected line emitters. In a total volume of ~ 90 physical Mpc^3 , we find 186 LAEs, 25 [O II], 13 [O III] emitters, and 8 AGN candidates.

Regarding the photometric properties, from the MUSE datacubes we produce (1) the optimally extracted (OE), (2) the classical pseudo-NB, (3) the continuum, and (4) the WL images centered on each candidate with a typical size of $30'' \times 30''$. The OE images are constructed by combining all voxels along the wavelength direction that are within the corresponding 3D mask of each detected object from the PSF- and continuum-subtracted MUSE datacubes. This image can be interpreted as a pseudo-NB with a spectral width optimized for the S/N of the candidate (see also Appendix A in Borisova et al. 2016b for a detailed comparison of the OE with the pseudo-NB images).

As we will discuss in the next section, the choice of the continuum image is very critical, especially because based on this image, we define a line emitter to be continuum (or not) detected. The ideal case would be the availability of *Hubble Space Telescope (HST)* images, but these are not available for these fields. We can, however, take advantage of our IFU datacubes and build the broadband continuum image. Hence, our approach was to create three continuum images by coadding different spectral ranges. For each field, we considered the spectral layers redward of their QSO Ly α emission, and the continuum images were created combining 800 (1000 \AA), 1600 (2000 \AA), and all (~ 3000 \AA) wavelength layers in the red part of the datacube. Finally, due to the limited

Table 2
Statistics of the Detected Emitters

	Detected Emitters	LAEs w/ Continuum	LAEs w/o Continuum	[O II] Emitters	[O III] Emitters	AGNs/Galaxies	Skyline Layers	
Bulb	Off-blue	10	2	4	...	1	3	...
	On-Source	22	7	11	2	...	2	...
	Off-red	14	1	9	4	14
Hammerhead	Off-blue	40	9	28	2	1	...	5
	On-Source	22	3	17	1	1
	Off-red	33	5	20	2	6	...	18
Q0055–269	Off-blue	4	...	4
	On-Source	13	7	5	1	17
	Off-red	10	2	2	3	1	2	21
Q1317–0507	Off-blue	8	4	1	3	20
	On-Source	7	3	1	2	...	1	1
	Off-red	6	1	3	1	1	...	27
Q1621–0042	Off-blue	8	3	4	1	17
	On-Source	2	...	2
	Off-red	8	3	3	1	1	...	28
Q2000–330	Off-blue	13	6	6	1	14
	On-Source	8	3	3	1	1	...	14
	Off-red	4	1	3	19
TOTAL	232	60	126	25	13	8	...	

Note. For the six fields, we list the number of detections obtained in both the on-source datacube (the one centered on the QSO Ly α redshift) and the two control samples (off-blue and off-red). Each datacube has a width of 200 Å in the spectral direction, with the exception of the Bulb off-blue sample, which, due to the (low) Ly α redshift of the AGN, has a width of 131 Å. The last column (skyline layers) indicates the number of masked layers in the datacube due to the presence of some residual skyline features.

coverage on the blue side of the QSO Ly α emission, we conservatively assumed a continuum slope of $\beta = -2$ ($f_\lambda \propto \lambda^\beta$ in wavelength space; Meurer et al. 1999) to take into account the shape of the continuum. Then, we took a global statistic of these continuum images while masking the sources in each field. Our final selection of the best continuum image was the deepest one of the three. From the tests performed on our data, the 2000 Å continuum image turned out to be the deepest, because its width represents the best spectral compromise able to minimize the contribution of the sky-residual layers.

3.4. Estimation of Our Detection Limits

In order to compute the minimum flux for which we would not be able to detect any candidates, we determine our detection limits for both the continuum and Ly α emission line using the standard deviation (std) of 100 random locations for each field in our sample. The std is calculated on the continuum and pseudo-NB Ly α images where we mask out all of the bright sources with special attention to the scattered light and halos of bright foreground stars. We explored successively larger apertures, with radii from 0''.2 to 2'' (including the PSF radius) and a 3σ clipping algorithm. We also compare these values with the results from pixel-by-pixel statistics, i.e., the theoretical photon count noise variance, to measure the level of systematics resulting from the sky and continuum subtraction. The typical surface brightness values obtained in a 10 hr datacube within an aperture of 1'' in diameter are of the order of $10^{-20} \text{ erg s}^{-1} \text{ cm}^{-2} \text{ Å}^{-1} \text{ arcsec}^{-2}$ in the case of the continuum and $10^{-19} \text{ erg s}^{-1} \text{ cm}^{-2} \text{ arcsec}^{-2}$ for the Ly α emission.

Figure 3 shows the distribution of the Ly α fluxes and luminosities of the selected LAE candidates.

4. Results

In this section, we present our sample of ~ 200 LAEs detected in our MUSE datacubes in the proximity of quasars and in the control regions within a total volume of ~ 90 physical Mpc³. In particular, we focus on the Ly α luminosities and EWs as functions of distance from the QSOs. The overall properties of the sample are presented in Table 5.

4.1. Ly α Flux Estimations

Given the recent findings of the extended and diffuse nature of the Ly α emission from LAEs (Wisotzki et al. 2016; Leclercq et al. 2017), measuring reliable Ly α fluxes is not a trivial task because it might depend on both the methodology and available data.

In our analysis, the Ly α fluxes were accurately computed from the curve-of-growth (C.o.G.) analysis (following Wisotzki et al. 2016; Drake et al. 2017) performed on the pseudo-NB image centered on the QSO Ly α wavelength with a width of 200 Å. By collapsing the corresponding spectral channels of the on-source datacube and assuming the *CubeEx* coordinates for each target, the Ly α C.o.G. was computed using the fluxes extracted from concentric circular annuli of increasing radii (in steps of 0''.2) up to 4''. This results in a reasonable value for the characterization of compact objects and their possible extended emission. The total Ly α flux of each object was then determined from the integrated value out to the radius where the surface brightness within a 0''.2 annulus is equal to or less than zero.

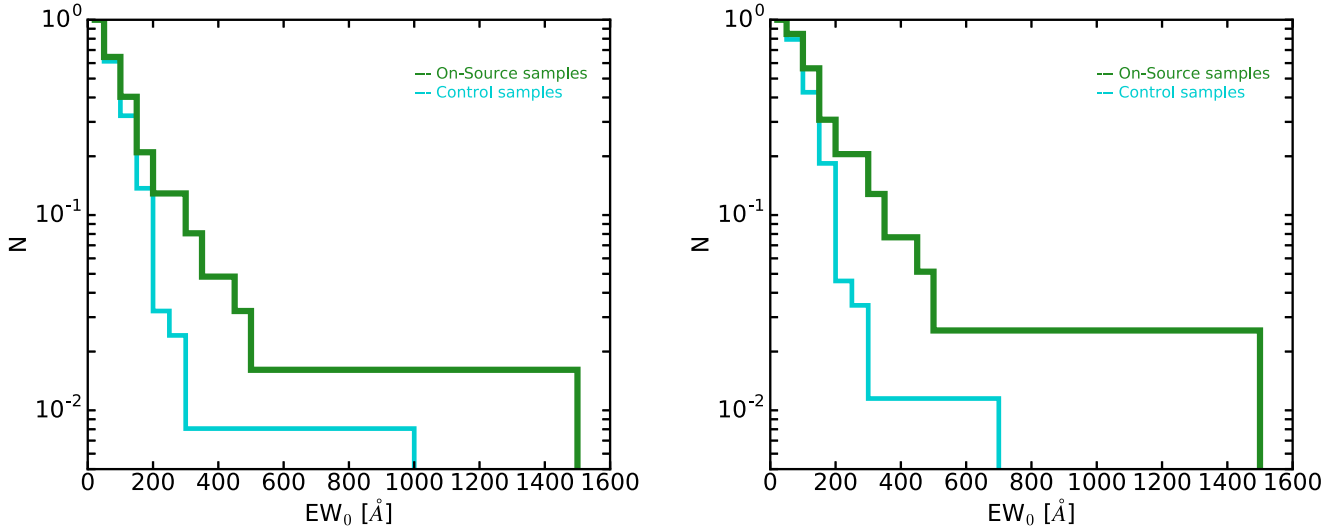


Figure 6. Cumulative rest-frame equivalent width (EW_0) distribution of all LAEs (left panel; all points in Figures 4 and 5) and the continuum-undetected LAEs (right panel; only arrow symbols in Figures 4 and 5). The cyan solid line represents the control sample distribution, while the green line marks the fluorescently illuminated QSO LAEs.

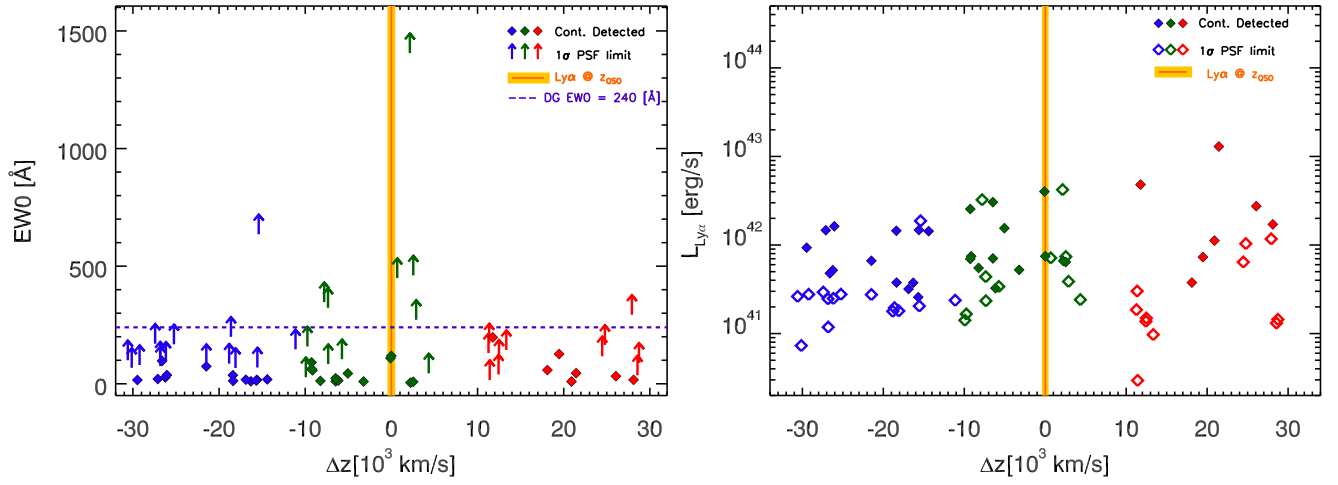


Figure 7. Stacked $EW_0(\text{Ly}\alpha)$ values (left) and $\text{Ly}\alpha$ luminosities (right) vs. the spectral distance (velocity) from the QSO for the fields at $z > 3.7$ (Q1317, Q0055, Q1621, Q2000). Symbols and colors are the same as for Figure 4, except in the case of the luminosity distribution where we use unfilled diamonds (instead of arrows) to plot the continuum-undetected LAEs.

Using the C.o.G. approach, we were able to recover LAEs as faint as $10^{-19} \text{ erg s}^{-1} \text{ cm}^{-2}$. Figure 3 shows the distribution of the $\text{Ly}\alpha$ fluxes and luminosities for each low-redshift field (Bulb in orange and Hammerhead in blue), for the high-redshift fields (in green), and for the full sample (in purple). Although there are definitely uncertainties and limitations in our calculations of $\text{Ly}\alpha$ fluxes, we stress that we have used exactly the same method for both the main and the control sample.

4.2. The Distribution of the $\text{Ly}\alpha$ EW

The EW is a quantitative way of describing the strength of spectral features, both in emission and absorption, compared to the continuum emission. Physically, EWs depend on the IMF and the gas metallicity from which stars form, as well as being a useful diagnostic to understand what kind of mechanisms are triggering and sustaining the SF (e.g., Schaerer 2002, 2003). Similar to the $\text{Ly}\alpha$ fluxes, the $\text{Ly}\alpha$ EW estimation is not unique, and it is very sensitive to the methodology used as well as to the data available for the EW measurements.

In general, we compute the EW as the following ratio:

$$EW(\text{Ly}\alpha) = \frac{\text{Flux}_{\text{Ly}\alpha}}{\text{Flux Density}_{\text{Continuum}}}, \quad (1)$$

where the numerator corresponds to the $\text{Ly}\alpha$ flux. $\text{Flux}_{\text{Ly}\alpha}$ is computed from the C.o.G. analysis, and it is in units of $\text{erg s}^{-1} \text{ cm}^{-2}$. The denominator is the continuum flux density measured in the MUSE continuum image (centered at $\lambda \sim 6000 \text{ \AA}$) and extrapolated to the wavelength of the line, assuming that the monochromatic fluxes f_ν of all objects are flat in frequency space. The unit in this case is $\text{erg s}^{-1} \text{ cm}^{-2} \text{ \AA}^{-1}$. However, as explained below, we will use different estimates of these fluxes depending on the nature of the analyzed object. The rest-frame $EW(\text{Ly}\alpha)$, $EW_0(\text{Ly}\alpha)$, is

$$EW_0(\text{Ly}\alpha) = \frac{EW(\text{Ly}\alpha)}{(1+z)}. \quad (2)$$

The redshift used in the above equation is defined as the flux centroid of the 3D segmentation mask associated with each

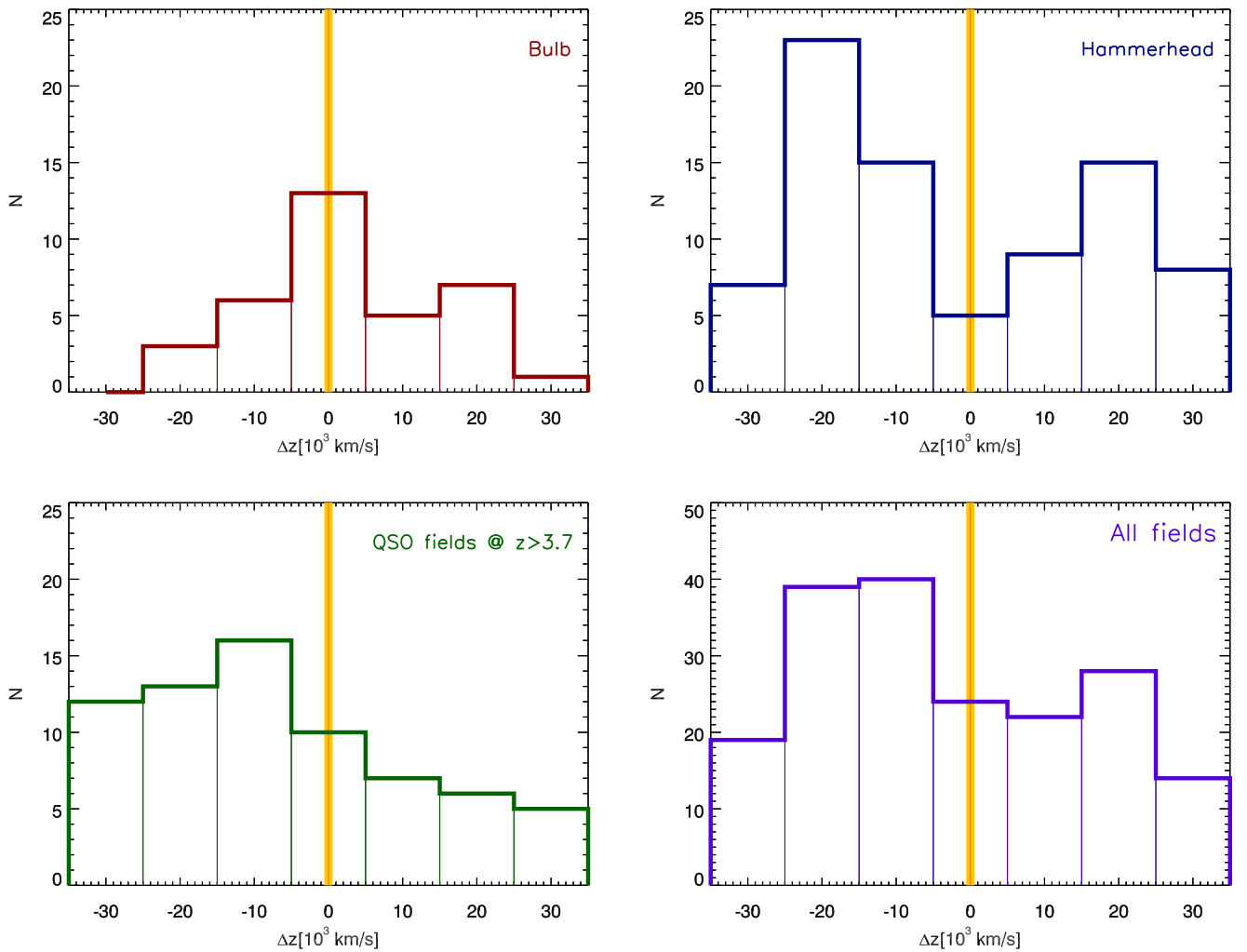


Figure 8. Ly α emitter (LAE) distribution as a function of the velocity separation with the QSO. The top panels show the Bulb (on the left) and Hammerhead (on the right) number densities while in the bottom-left panel the results for the MUSE $z > 3.7$ sample are shown. The LAE distribution of all MUSE fields is shown in the bottom-right panel.

detected object. Stellar population synthesis models predict that in the case of continuously star-forming galaxies, the $EW_0(\text{Ly}\alpha)$ produced by Population II stars (hereafter PopII stars) cannot be higher than 240 Å except in very extreme cases (Charlot & Fall 1993; Schaerer 2002). $EW_0(\text{Ly}\alpha)$ values above this value may in principle be expected for metal-free PopIII stellar systems (Schaerer 2003; Raiter et al. 2010) and/or DGs (C12).

In order to compute the $EW_0(\text{Ly}\alpha)$ of our targets, we decide to follow two different approaches depending on the detection (or not) of our LAE in the continuum image. First, in order to establish whether our LAE is detected in the continuum, we measure the continuum flux of our target as the maximum value obtained from the measured continuum flux in nine different and contiguous positions around the central coordinates of the targets within an aperture with radius equal to the PSF size. This method takes into account possible offsets between the spatial peak of the Ly α emission and the stellar continuum (note that the PSF values, listed in Table 1, are all larger than the offsets proposed in Shibuya et al. 2014). Second, if the continuum flux of the target within the PSF size aperture, $F_{\text{Cont}@PSF}$, is higher than three times the std of the continuum image ($3\sigma_{\text{Cont}}$, i.e., the local noise; see Section 3.4

for a detailed explanation of how we computed this value), the LAE is considered detected in the continuum. In the case of $F_{\text{Cont}@PSF} < 3\sigma_{\text{Cont}}$, our LAE is considered continuum undetected. Of the 186 LAEs selected in our sample, 54% were undetected in the continuum. In the fourth and fifth columns of Table 2, this statistic is provided for each field.

In the case of the continuum-detected (CD) LAEs, we used the matched-aperture approach as in C12, and the $EW_0(\text{Ly}\alpha)$ is computed as follows:

$$EW_0(\text{Ly}\alpha)|_{\text{CD}} = \frac{\text{Flux}_{\text{Ly}\alpha}(R)}{\text{Flux}_{\text{Cont}}(R) + 1\sigma(R)} \times \frac{1}{(1+z)}, \quad (3)$$

where $\text{Flux}_{\text{Ly}\alpha}(R)$ is the Ly α flux within the radius R derived from the C.o.G. analysis, $\sigma(R)$ is the std of the continuum scaled to the same R apertures, and $\text{Flux}_{\text{Cont}}(R)$ is the continuum flux measured in the same aperture as the Ly α flux. We also masked the contribution of the visible bright continuum objects that were contaminating the measurements extracted from the target aperture, as well as possible contamination from fainter foreground objects inside the aperture.

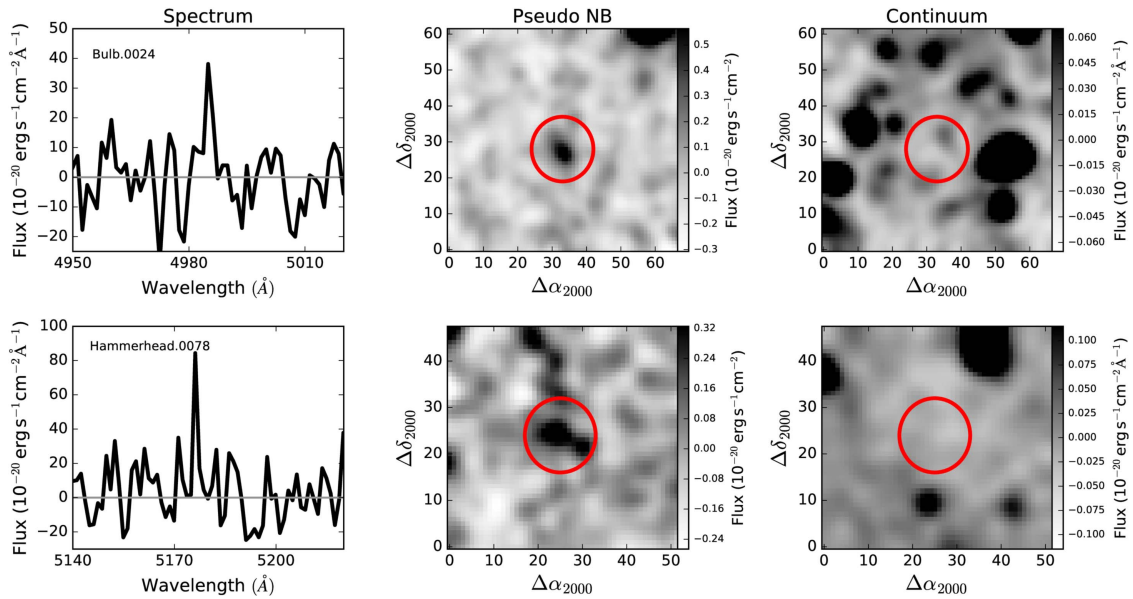


Figure 9. Dark Galaxy candidates detected in the MUSE $z < 3.2$ fields. Left: the MUSE spectrum within a wavelength range highlighting the observed Ly α emission. The spectrum has been smoothed with a 2 pixel Gaussian filter. Middle: the MUSE Ly α pseudo-narrowband image is shown. The position of the candidate is marked by the red circle. The image was smoothed using a 2 pixel Gaussian kernel, and the Ly α flux is shown in z -scale. Right: continuum broadband image obtained from the MUSE datacube. We applied a Gaussian smoothing with a 2 pixel radius. The continuum flux is plotted with a z -scale stretch between $\pm 5\sigma$. In each panel, north is up and east is left. Plate scale is $0''/2/\text{pix}$.

For those LAEs undetected in the continuum image (CU), we used the PSF-aperture approach, and $EW_0(\text{Ly}\alpha)$ is obtained via

$$EW_0(\text{Ly}\alpha)|_{\text{CU}} = \frac{\text{Flux}_{\text{Ly}\alpha}(R)}{\max[1\sigma_{\text{Cont}}, \text{Flux}_{\text{Cont}}(R_{\text{PSF}}) + 1\sigma_{\text{Cont}}]} \times \frac{1}{(1+z)}, \quad (4)$$

where $\text{Flux}_{\text{Ly}\alpha}(R)$ is derived as in the case of the CD LAEs, and here the continuum flux is computed using the one in the PSF aperture plus 1σ . This method proposed by Feldman & Cousins (1998) ensures an upper limit for the continuum estimation, if the flux in the PSF aperture is positive; otherwise, the continuum flux is at least 1σ . This upper limit in the continuum will yield a lower limit in the estimation of the EW_0 .

Despite the complexity and the limitations in estimating the EW_0 , we would like to stress here that we are more interested in the relative distribution of the EW_0 values around the QSOs rather than in their absolute values. Similarly to any other measured properties of the LAEs in our sample, we have used exactly the same methods to estimate the EW_0 independent of the position of the object relative to the quasar redshift, both in the main and in the control samples.

In Figures 4 and 5, we present the measured $EW_0(\text{Ly}\alpha)$ values and limits as a function of the redshift difference (spectral distance) from the QSO for the low- and high-redshift samples, respectively. The vertical yellow shaded area represents the position of the QSO, while the gray lines indicate the masked position of the OH skylines. The CD LAEs are plotted with diamond symbols, while the arrows symbolize the lower limit $EW_0(\text{Ly}\alpha)$ estimations for the CU LAEs. Green colors represent the LAEs detected in the on-source (QSO) samples, while the blue and red ones indicate the control samples. The horizontal dashed line at 240 \AA denotes the $EW_0(\text{Ly}\alpha)$ limit expected for “normal” star-forming galaxies. In all MUSE high- z fields, we clearly see a higher occurrence

of objects with $EW_0(\text{Ly}\alpha) > 240 \text{ \AA}$ closer to the QSOs rather than in the control samples. For a first, qualitative assessment of the global, cumulative $EW_0(\text{Ly}\alpha)$ distribution in proximity of the QSOs compared to the control sample, we used the EW_0 lower limits as a (conservative) value for the EW_0 of the CU objects. In the left-hand panel of Figure 6, the green line indicates the $EW_0(\text{Ly}\alpha)$ cumulative distribution of all (CD and CU) LAEs detected around the QSO. The cyan line denotes the detections in the control samples. In the right-hand panel, we plot the same but for the CU LAEs. It is clear in both cases that for $EW_0(\text{Ly}\alpha) > 240 \text{ \AA}$, the number of LAEs in the on-source samples is higher (see Figure 7). How statistically significant is this difference? In the limits mentioned above, we quantified the probability that the on-source and the control samples are drawn from the same parent population using two nonparametric statistical tests: the Anderson–Darling (AD) test, which is more sensitive to the tails of the distribution, and the Kolmogorov–Smirnov (KS) test, which is more sensitive to the center of the distribution. We stress that these tests are only valid in the assumption that the EW_0 lower limits are the true values for the CU objects. This is a conservative assumption because true DG objects could have a much higher EW_0 than normal LAEs. To avoid mixing true measurements with these limits, we limit the comparison to the CU LAEs (right panel of Figure 6), and we obtain p -values of about 0.001 in both KS and AD tests. Such low p -values strongly suggest that we can reject the null hypothesis that the two samples belong to the same population, hence the on-source and the control samples are statistically different, in the limits mentioned above. We also stress that other statistics, such as survival analysis, would not work in our cases since the CU candidates consist by design only of lower limits. Indeed, a Kaplan–Meier estimator would return a flat cumulative distribution function. Another possibility is to compare the measured Ly α fluxes—the nominator in the EW_0 definition—of the CU objects around QSOs and in the control sample under the assumption that a

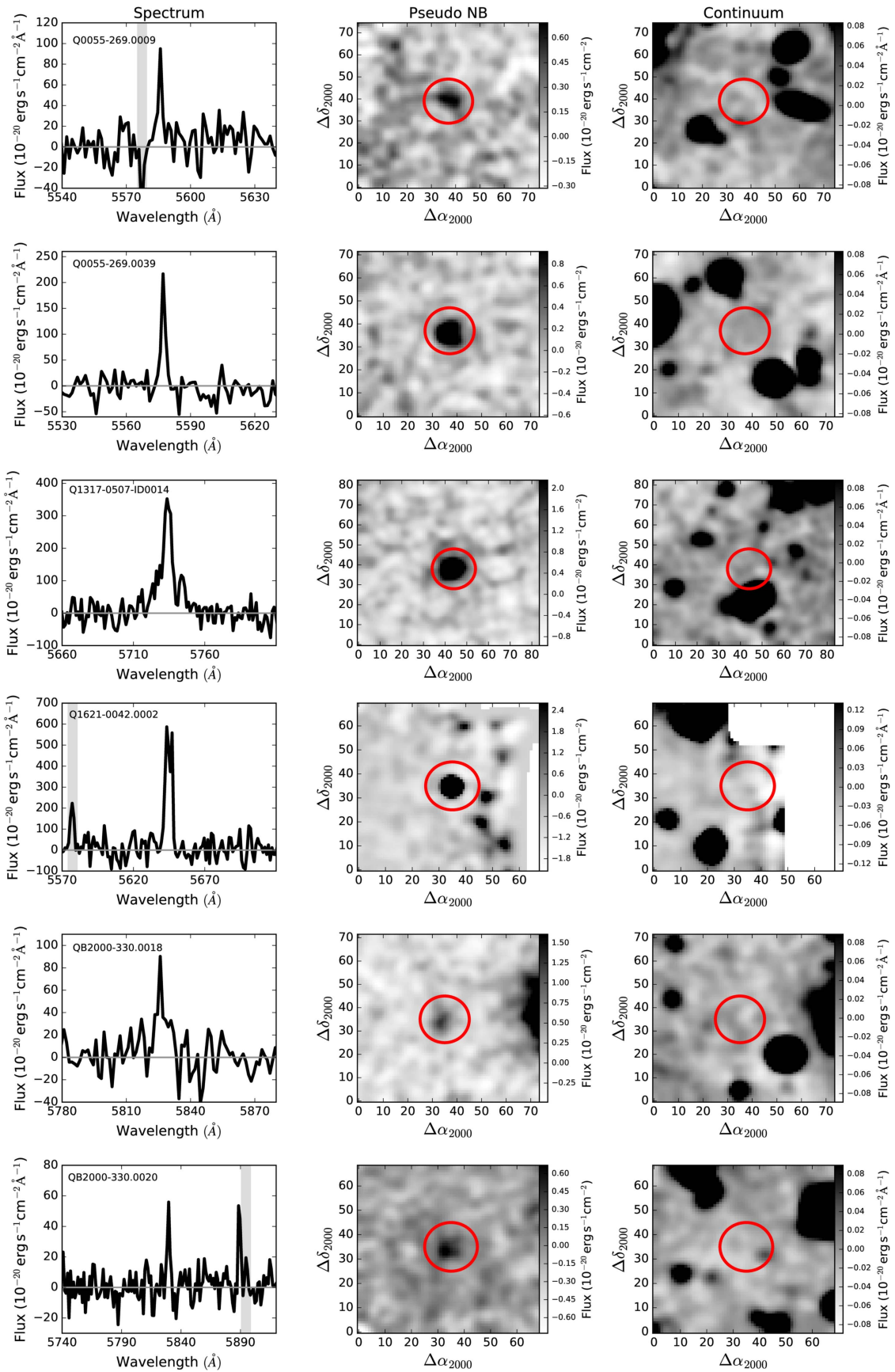


Figure 10. Dark Galaxy candidates detected in the MUSE QSO $z > 3.7$ fields. Panels have the same meaning as in Figure 9.

Table 3
Derived Properties of the Dark Galaxy Candidates

Field	ID	R.A. (J2000)	Decl. (J2000)	Area (pixels ²)	$\lambda_{\text{detected}}$ (Å)	Redshift	Flux(Ly α) ^a (10^{-17} erg s ⁻¹ cm ⁻²)	$L(\text{Ly}\alpha)$ (10^{41} erg s ⁻¹)	Flux(Cont _{PSF}) ^b (10^{-20} erg s ⁻¹ cm ⁻² Å ⁻¹)	EW ₀ (Ly α) ^c (Å)	$M_{\text{gas}}^{\text{d}}$ ($10^9 M_{\odot}$)
Bulb	24	04:22:02.904	-38:37:43.71	41	4984.50	3.102	0.16 ± 0.01	1.35	-0.02 ± 0.14	>265	0.2
Hammerhead	78	23:21:14.776	01:36:02.12	49	5175.52	3.259	0.29 ± 0.02	2.82	0.10 ± 0.27	>253	0.4
Q0055-269	9	00:58:00.108	-26:43:26.42	98	5585.45	3.596	0.35 ± 0.02	4.40	0.05 ± 0.24	>323	0.6
Q0055-269	39	00:57:57.721	-26:42:57.52	121	5665.77	3.662	0.55 ± 0.02	7.14	0.08 ± 0.26	>450	1.0
Q1317-0507	14	13:20:29.317	-05:23:52.02	314	5732.48	3.717	3.12 ± 0.06	42.1	0.26 ± 0.47	>1406	5.9
Q1621-0042	2	16:21:14.791	-00:42:26.18	71	5644.02	3.644	2.52 ± 0.05	32.4	1.12 ± 1.56 ^e	>347	4.5
Q2000-330	18	20:03:24.882	-32:51:46.95	81	5825.74	3.794	0.52 ± 0.02	7.38	0.04 ± 0.24	>461	1.0
Q2000-330	20	20:03:25.213	-32:52:04.57	55	5829.11	3.797	0.27 ± 0.02	3.87	0.01 ± 0.21	>272	0.5

Notes.

^a The Ly α flux is computed from the curve-of-growth analysis detailed in Section 4.3.

^b The continuum flux is computed as the maximum between the fluxes measured in nine adjacent PSF size apertures, i.e., it will be always positive.

^c The rest-frame EWs were determined using the PSF-aperture approach; see Equation (4).

^d The gas masses are computed using Equation (8) in C12.

^e This measurement is relatively high due to the position of this target on the edge of the FoV.

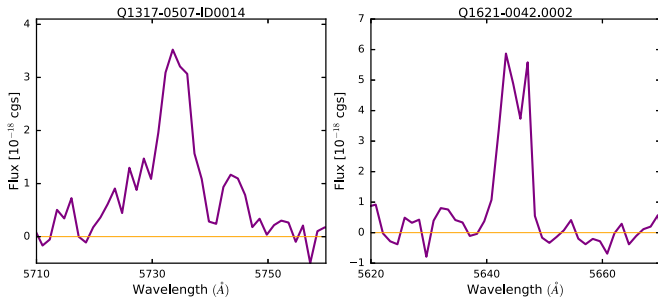


Figure 11. Zoomed-in portion of the Ly α line profile for the double-peaked dark galaxy candidates. Fluxes are given in units of 10^{-18} erg s $^{-1}$ cm $^{-2}$ \AA^{-1} .

significant fraction of CU sources around the QSOs are boosted by fluorescence. In this case, KS and AD tests reject the null hypothesis that the Ly α flux distribution of these sources is similar to the control sample with $p_{\text{KS}} = 0.035$ and $p_{\text{AD}} = 0.042$. Although higher than the p -values obtained by comparing the EW_0 distributions, this is an additional supporting evidence that CU LAEs around the QSOs are different than in the control sample. This is not due to environmental differences for which galaxies would be generally brighter around the QSOs. Indeed, performing KS and AD tests on the continuum-detected sources around QSOs and in the control sample, we obtain $p_{\text{KS}} = 0.528$ and $p_{\text{AD}} = 0.590$, strongly suggesting that normal galaxies are similar in our “on-source” and control samples.

Similarly, the excess of high- EW_0 objects is not connected to an apparent enhancement in the number density of LAEs in the proximity of the quasars with respect to the control fields, as shown in Figure 8, where we plot the distribution of the LAEs as a function of the distance from the central ionizing source (an AGN in the case of the Bulb field and QSOs for the others). With the exception of the Bulb field, which hosts a lower-luminosity AGN, we do not find evidence for an overdensity of LAEs around any of the MUSE QSOs, although the statistical sample is small. Our result is in agreement with the recent findings of Uchiyama et al. (2018) using a sample of ~ 150 QSOs and of Kikuta et al. (2017) using ~ 300 LAEs in different environments.

We will discuss in Section 5 the implication of these results in light of our search for DG candidates fluorescently illuminated by the quasars.

4.3. High- EW_0 Sources

As shown in the previous section, 11 of the ~ 200 LAEs in the total volume explored in this study, including the control samples, present a lower limit on their $\text{EW}_0(\text{Ly}\alpha)$ larger than 240 \AA (arrows in Figures 4 and 5 above the purple horizontal dashed line). We have demonstrated that these high- EW_0 objects tend to be more frequent in the proximity of the quasars and in our high-redshift sample. In particular, six of these are detected in our on-source subcubes around the four high-redshift quasars, representing about 25% of the total detected LAEs (24) in this volume. This value is significantly larger than the corresponding fraction in the control samples for the high-redshift quasars (about 4%) and for the two fields at low redshift.

In total, eight high- EW_0 objects are present in the on-source samples, i.e., within 10^4 km s $^{-1}$ from the quasars (AGN in the case of the Bulb). In Figures 9 and 10, we show the spectra and postage stamps of these eight high- EW_0 objects detected in the

low- and high-redshift samples, respectively. In particular, for each target, the left panel illustrates a zoom-in of the MUSE spectrum around the detected Ly α emission line, while the central and right panels specifically show the Ly α pseudo-NB and continuum images obtained from the MUSE datacubes. The position of each object is indicated with a red circle. Their Ly α emission appear compact, similarly to their analogues detected at $z \approx 2.4$ by C12. Coordinates, derived photometric and spectral properties, as well as EW_0 lower limits, are reported in Table 3.

The Ly α line profiles of these sources are typically asymmetric, and in two cases, highlighted in Figure 11, the emission appears double peaked. Since the shape of the Ly α profile may be sensitive to the gas kinematics, HI geometry, and dust content, our plan is to further investigate these two double-peaked high- EW_0 sources as well as the ~ 60 double-peaked LAEs in our total sample with the help of radiative transfer models in a separate paper.

The main properties of the three high- EW_0 sources in our control samples are summarized in Table 4, and their postage stamps are shown in Figure 12. We note that these objects do not show any other prominent lines in their spectra. When we considered the 3D extension, i.e., spatial and spectral pixels detected above a threshold, we do not find any significant difference between the eight objects near to the AGN/QSO and these three high- EW_0 objects.

5. Discussion

The most prominent and characteristic feature of quasar fluorescent illumination is a boost in the $\text{EW}_0(\text{Ly}\alpha)$ of LAEs, leading to (i) a higher frequency of objects without continuum counterparts and (ii) EW_0 limits above 240 \AA with respect to “blank fields” (e.g., Cantalupo et al. 2005, 2007; C12). Because the measurement of EW_0 relies on different methodologies in the literature and because of the different observational techniques and instruments, a proper comparison between the EW_0 of LAEs detected in “quasar fields” and “blank fields” has been difficult in previous surveys.

Thanks to the new MUSE Integral Field Spectrograph, we were able to obtain a homogeneous sample of Ly α emitting sources around six AGN/QSOs at $z > 3.2$, and we were able to build control samples using the same data, and the same data reduction and analysis techniques.

As expected in the case of fluorescent illumination, we detected an overall excess of high- EW_0 sources in the proximity of the quasars with respect to the control samples (Figures 4 and 5). We stress again that, despite the uncertainties and limitations on the measurement of absolute values or limits for the EW_0 , we have used exactly the same methods for our estimates for each source independent of its distance from the quasar.

The excess of high- EW_0 sources is more prominent in the four quasar fields at $z \sim 3.7$. The field-to-field variations could be possibly due to the relatively small MUSE FoV and limited volume probed around each individual quasar. However, they could also suggest intrinsic differences in the quasar properties, such as, e.g., opening angle or age. In any case, as demonstrated in Section 4.2, the EW_0 distribution in the combined sample around the quasars (on-source) is statistically different from the EW_0 distribution in the control samples at a high significance level.

Table 4
Derived Properties of Ly α Candidates with EW $_0 > 240 \text{ \AA}$ Detected in the Control Samples

Field	ID	R.A. (J2000)	Decl. (J2000)	Area (pixels ²)	$\lambda_{\text{detected}}$ (\AA)	Redshift	Flux(Ly α) ($10^{-17} \text{ erg s}^{-1} \text{ cm}^{-2}$)	$L(\text{Ly}\alpha)$ ($10^{41} \text{ erg s}^{-1}$)	Flux(Cont _{PSF}) ($10^{-20} \text{ erg s}^{-1} \text{ cm}^{-2} \text{ \AA}^{-1}$)	EW $_0(\text{Ly}\alpha)$ (\AA)
Bulb	22	04:21:59.656	-38:37:39.14	105	5182.19	3.264	0.28 ± 0.01	2.77	0.03 ± 0.17	>370
Q0055-269	6	00:57:59.131	-26:43:10.75	149	5504.99	3.530	1.57 ± 0.04	18.7	0.36 ± 0.55	>636
Q2000-330	7	20:03:23.891	-32:51:58.87	132	6079.46	4.001	0.73 ± 0.03	11.7	0.30 ± 0.50	>293

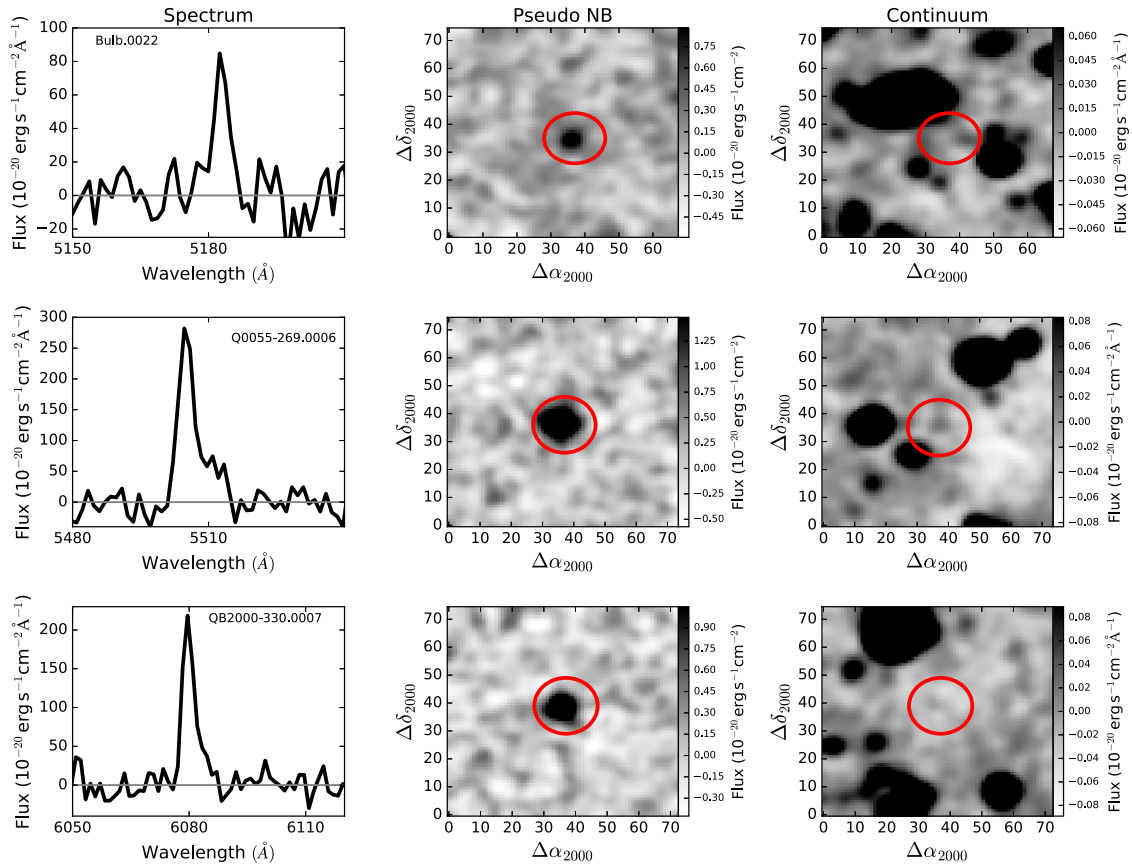


Figure 12. High- EW_0 objects detected in the control samples. Panels have the same meaning as in Figure 9.

Is there any other mechanism intrinsic to the sources that would enhance the $EW_0(\text{Ly}\alpha)$ in the proximity of quasars without the need for fluorescent “illumination”? High values of EW_0 , if intrinsic, may be due to a younger stellar population, different IMFs, or lower metallicities (see, e.g., Charlot & Fall 1993; Malhotra & Rhoads 2002; Schaerer 2002; Krumholz & Dekel 2012; Orsi et al. 2012). In order for these processes to produce an excess of high- EW_0 sources in the proximity of the quasar, a relation between the quasar environment and intrinsic galaxy properties would be required. We have explored if the $\text{Ly}\alpha$ luminosity and the number density of the CD galaxies (therefore not DG candidates) are different in the proximity of the quasar, possibly indicating a different “environment,” but we have found no statistically different results between the on-source and the control samples with respect to these quantities. Moreover, the compact $\text{Ly}\alpha$ morphology and the isolated nature of our high- EW_0 objects do not suggest any possible effects due to merger activities, although our spatial resolution and the lack of *HST* imaging would not allow us to detect interactions below scales of a few kiloparsecs. Although we cannot categorically rule out such a possibility, we see no reason to favor it.

In contrast, the high luminosities of our quasars, the demonstrated existence of the “quasar proximity effect” in absorption (at least along our line of sight; Carswell et al. 1982; Dall’Aglio et al. 2008; Calverley et al. 2011), and the detection of bright $\text{Ly}\alpha$ nebulae around these quasars (Borisova et al. 2016b; R. A. Marino et al. 2018, in preparation), which demonstrates that quasars are illuminating their surroundings, all suggest that QSO fluorescence is the most likely explanation

for the excess of compact high- EW_0 sources correlated with the quasar redshift in our survey.

In this case, the eight high- EW_0 sources without detectable continuum counterparts and EW_0 limits larger than 240 \AA are the best candidates for DGs fluorescently illuminated by the QSOs in our survey. The number densities, luminosities, and morphologies of these sources are very similar to their 12 analogues detected by C12 at $z \approx 2.4$ using NB imaging around a single bright QSO.

How many of these sources have intrinsically high EW_0 without the need for fluorescent “illumination”? Let us consider the fraction of high- EW_0 sources in our on-source and control sample at different redshifts. The combined high-redshift sample has 25% high- EW_0 objects on-source and only about 5% in the control sample, suggesting that about one to two of the six high-redshift LAEs with EW_0 limits above 240 \AA could be objects with intrinsically high EW_0 . Our fraction of 5% high- EW_0 objects away from quasars at $z \sim 3.6$ is consistent with other studies, despite the different methodologies used to measure the EW_0 . For instance, Hashimoto et al. (2017) measured a fraction of about 3% high- EW_0 objects in the Hubble Ultra Deep Field using deep MUSE $\text{Ly}\alpha$ datacubes and the deepest *HST* continuum measurements available to date. Despite the small number statistics, this suggests that a significant fraction of the eight sources with EW_0 limits above 240 \AA and without continuum counterparts in our survey are strong candidates for DGs detected at $z > 3$.

From the luminosities of these sources and following the approach of C12, we can estimate their total gas masses and star formation efficiencies ($\text{SFEs} = \text{SFR}/M_{\text{gas}}$). In particular,

Table 5
Physical Properties of the Ly α Candidates

Field	ID	Area (pixels ²)	Redshift	Flux(Ly α) (10 ⁻¹⁷ erg s ⁻¹ cm ⁻²)	L (Ly α) (10 ⁴¹ erg s ⁻¹)	Flux(Cont _{PSF}) (10 ⁻²⁰ erg s ⁻¹ cm ⁻² Å ⁻¹)	EW ₀ (Ly α) (Å)
Bulb	15b	225	2.9	1.53 ± 0.04	11.5	1.83 ± 0.60	96 ± 32
Bulb	30b	39	3.0	0.11 ± 0.01	0.88	0.17 ± 0.31	>93
Bulb	34b	88	3.0	0.09 ± 0.01	0.72	-0.07 ± 0.14	>162
Bulb	36b	50	3.0	0.13 ± 0.01	0.99	0.21 ± 0.35	>90
Bulb	40b	49	3.0	0.12 ± 0.01	0.94	0.12 ± 0.26	>112
Bulb	41b	303	3.0	3.37 ± 0.06	27.0	2.09 ± 0.70	101 ± 34
Bulb	2q	47	3.0	0.09 ± 0.01	0.73	0.35 ± 0.49	>46
Bulb	4q	45	3.0	0.09 ± 0.01	0.79	3.91 ± 0.16	6 ± 1
Bulb	6q	45	3.0	0.11 ± 0.01	0.89	0.04 ± 0.19	>140
Bulb	8q	121	3.1	0.91 ± 0.03	7.64	1.29 ± 0.45	13 ± 5
Bulb	9q	306	3.1	2.89 ± 0.05	24.3	3.61 ± 0.72	198 ± 39
Bulb	14q	36	3.1	0.06 ± 0.01	0.53	3.61 ± 0.18	5 ± 1
Bulb	15q	55	3.1	0.20 ± 0.01	1.74	0.14 ± 0.29	>173
Bulb	19q	52	3.1	0.12 ± 0.01	1.01	0.18 ± 0.33	>87
Bulb	22q	248	3.1	2.41 ± 0.05	20.6	3.08 ± 0.59	60 ± 12
Bulb	25q	74	3.1	0.15 ± 0.01	1.30	0.09 ± 0.23	>155
Bulb	26q	39	3.1	0.12 ± 0.01	1.04	4.08 ± 0.26	6 ± 1
Bulb	28q	44	3.1	0.10 ± 0.01	0.88	0.18 ± 0.33	>74
Bulb	29q	40	3.1	0.14 ± 0.01	1.22	0.16 ± 0.30	>111
Bulb	32q	39	3.1	0.18 ± 0.01	1.59	0.48 ± 0.27	21 ± 12
Bulb	34q	43	3.1	0.08 ± 0.01	0.74	0.02 ± 0.16	>121
Bulb	36q	174	3.2	0.39 ± 0.02	3.56	0.43 ± 0.57	>165
Bulb	38q	53	3.2	0.08 ± 0.01	0.78	0.29 ± 0.44	>47
Bulb	3r	41	3.2	0.05 ± 0.01	0.49	0.34 ± 0.48	>26
Bulb	6r	41	3.2	0.04 ± 0.01	0.36	0.20 ± 0.34	>27
Bulb	9r	35	3.2	0.08 ± 0.01	0.73	0.05 ± 0.19	>95
Bulb	11r	69	3.2	0.11 ± 0.01	1.03	0.12 ± 0.27	>96
Bulb	21r	46	3.3	0.13 ± 0.01	1.24	0.21 ± 0.35	>85
Bulb	28r	44	3.3	0.07 ± 0.01	0.69	-0.20 ± 0.14	>114
Bulb	39r	34	3.3	0.22 ± 0.01	2.19	0.53 ± 0.23	19 ± 8
Bulb	82r	38	3.3	0.07 ± 0.01	0.75	0.38 ± 0.53	>33
Bulb	83r	57	3.3	0.22 ± 0.01	2.22	0.24 ± 0.38	>130
Hammerhead	3b	37	2.9	0.37 ± 0.02	2.87	1.03 ± 0.64	>147
Hammerhead	6b	41	3.0	0.09 ± 0.01	0.72	1.75 ± 0.46	6 ± 2
Hammerhead	8b	48	3.0	0.35 ± 0.02	2.72	3.94 ± 0.50	14 ± 2
Hammerhead	11b	44	3.0	0.21 ± 0.02	1.65	0.42 ± 0.40	>134
Hammerhead	12b	33	3.0	0.25 ± 0.02	1.93	1.42 ± 0.79	>78
Hammerhead	14b	43	3.0	0.13 ± 0.01	1.01	0.52 ± 0.43	>75
Hammerhead	15b	56	3.0	0.18 ± 0.01	1.39	0.42 ± 0.40	>112
Hammerhead	18b	39	3.0	0.17 ± 0.01	1.38	5.90 ± 0.45	4 ± 1
Hammerhead	19b	37	3.0	0.17 ± 0.01	1.36	4.42 ± 0.44	7 ± 1
Hammerhead	22b	41	3.0	0.14 ± 0.01	1.09	0.49 ± 0.42	>80
Hammerhead	23b	38	3.0	0.18 ± 0.01	1.45	0.03 ± 0.24	>191
Hammerhead	28b	53	3.0	0.07 ± 0.01	0.55	4.90 ± 0.53	3 ± 1
Hammerhead	30b	79	3.0	0.31 ± 0.02	2.51	0.35 ± 0.37	>211
Hammerhead	34b	47	3.0	0.08 ± 0.01	0.68	0.37 ± 0.37	>56
Hammerhead	36b	47	3.0	0.13 ± 0.01	1.02	0.17 ± 0.29	>108
Hammerhead	42b	46	3.0	0.25 ± 0.02	2.00	0.78 ± 0.54	>114
Hammerhead	45b	29	3.0	0.16 ± 0.01	1.29	0.95 ± 0.61	>65
Hammerhead	46b	42	3.0	0.15 ± 0.01	1.20	0.56 ± 0.45	>81
Hammerhead	47b	51	3.0	0.31 ± 0.02	2.51	0.97 ± 0.62	>124
Hammerhead	48b	43	3.0	0.16 ± 0.01	1.30	0.84 ± 0.56	>70
Hammerhead	49b	44	3.0	0.11 ± 0.01	0.93	1.14 ± 0.68	>41
Hammerhead	53b	40	3.0	0.28 ± 0.02	2.31	0.89 ± 0.58	>119
Hammerhead	56b	50	3.0	0.32 ± 0.02	2.63	0.85 ± 0.57	>140
Hammerhead	60b	84	3.0	0.03 ± 0.01	0.27	0.37 ± 0.38	>21
Hammerhead	64b	73	3.0	0.30 ± 0.02	2.50	0.43 ± 0.40	>184
Hammerhead	66b	67	3.0	0.11 ± 0.01	0.93	0.90 ± 0.58	>47
Hammerhead	72b	80	3.1	0.43 ± 0.02	3.63	1.11 ± 0.67	>158
Hammerhead	74b	75	3.1	0.23 ± 0.02	1.93	0.69 ± 0.50	>113
Hammerhead	78b	43	3.1	0.02 ± 0.01	0.17	2.02 ± 0.47	4 ± 1
Hammerhead	81b	33	3.1	0.50 ± 0.02	4.19	1.46 ± 0.81	>151
Hammerhead	83b	224	3.1	1.76 ± 0.04	14.9	7.77 ± 1.06	14 ± 2

Table 5
(Continued)

Field	ID	Area (pixels ²)	Redshift	Flux(Ly α) (10 ⁻¹⁷ erg s ⁻¹ cm ⁻²)	L(Ly α) (10 ⁴¹ erg s ⁻¹)	Flux(Cont _{PSF}) (10 ⁻²⁰ erg s ⁻¹ cm ⁻² Å ⁻¹)	EW ₀ (Ly α) (Å)
Hammerhead	84b	221	3.1	1.99 ± 0.04	16.8	16.2 ± 1.1	8 ± 1
Hammerhead	87b	36	3.1	0.27 ± 0.02	2.30	0.46 ± 0.41	>162
Hammerhead	89b	41	3.1	0.24 ± 0.02	2.03	1.33 ± 0.76	>77
Hammerhead	91b	37	3.1	0.17 ± 0.01	1.44	2.25 ± 0.44	7 ± 1
Hammerhead	95b	45	3.1	0.18 ± 0.01	1.58	0.41 ± 0.39	>114
Hammerhead	118b	50	3.1	0.13 ± 0.01	1.17	1.19 ± 0.70	>46
Hammerhead	1q	65	3.1	0.36 ± 0.02	3.17	1.11 ± 0.67	>131
Hammerhead	2q	50	3.1	0.10 ± 0.01	0.91	1.19 ± 0.70	>36
Hammerhead	7q	34	3.1	0.13 ± 0.01	1.17	0.03 ± 0.24	>135
Hammerhead	11q	47	3.1	0.12 ± 0.01	1.03	0.74 ± 0.53	>53
Hammerhead	14q	59	3.1	0.13 ± 0.01	1.16	1.28 ± 0.74	>42
Hammerhead	15q	35	3.1	0.20 ± 0.01	1.78	1.29 ± 0.74	>65
Hammerhead	17q	46	3.1	0.19 ± 0.01	1.68	0.56 ± 0.45	>100
Hammerhead	18q	59	3.1	0.19 ± 0.01	1.68	0.27 ± 0.33	>135
Hammerhead	28q	63	3.2	0.15 ± 0.01	1.35	0.41 ± 0.39	>91
Hammerhead	30q	39	3.2	0.22 ± 0.01	1.98	2.05 ± 0.45	3 ± 1
Hammerhead	38q	42	3.2	0.12 ± 0.01	1.10	0.47 ± 0.41	>68
Hammerhead	42q	432	3.2	6.68 ± 0.08	62.8	44.8 ± 1.48	18 ± 1
Hammerhead	59q	42	3.2	0.17 ± 0.01	1.59	0.14 ± 0.28	>140
Hammerhead	63q	44	3.2	0.11 ± 0.01	1.10	0.62 ± 0.47	>57
Hammerhead	64q	75	3.2	0.28 ± 0.02	2.70	0.71 ± 0.51	>129
Hammerhead	71q	49	3.2	0.28 ± 0.02	2.71	1.49 ± 0.82	>80
Hammerhead	72q	90	3.2	0.24 ± 0.02	2.39	2.11 ± 0.64	9 ± 3
Hammerhead	77q	49	3.2	0.21 ± 0.01	2.02	0.77 ± 0.54	>90
Hammerhead	81q	118	3.2	0.10 ± 0.01	1.03	0.44 ± 0.40	>61
Hammerhead	12r	41	3.3	0.14 ± 0.01	1.43	1.25 ± 0.73	>45
Hammerhead	15r	41	3.3	0.07 ± 0.01	0.71	0.39 ± 0.38	>42
Hammerhead	19r	39	3.3	0.14 ± 0.01	1.44	2.74 ± 0.45	3 ± 1
Hammerhead	22r	51	3.3	0.14 ± 0.01	1.48	0.64 ± 0.48	>70
Hammerhead	23r	47	3.3	0.21 ± 0.01	2.15	0.95 ± 0.61	>80
Hammerhead	27r	38	3.3	0.14 ± 0.01	1.48	0.78 ± 0.54	>62
Hammerhead	29r	46	3.3	0.14 ± 0.01	1.44	0.97 ± 0.61	>52
Hammerhead	32r	97	3.3	0.30 ± 0.02	3.08	1.27 ± 0.74	>94
Hammerhead	33r	57	3.3	0.11 ± 0.01	1.19	2.31 ± 0.55	8 ± 2
Hammerhead	34r	45	3.3	0.18 ± 0.01	1.91	1.20 ± 0.71	>60
Hammerhead	38r	191	3.3	0.74 ± 0.03	7.74	1.67 ± 0.89	>190
Hammerhead	43r	47	3.4	0.07 ± 0.01	0.73	1.50 ± 0.83	>19
Hammerhead	55r	42	3.4	0.37 ± 0.02	3.99	1.46 ± 0.81	>106
Hammerhead	60r	52	3.4	0.07 ± 0.01	0.72	-0.02 ± 0.23	>68
Hammerhead	61r	46	3.4	0.22 ± 0.02	2.35	0.49 ± 0.42	>119
Hammerhead	63r	58	3.4	0.58 ± 0.02	6.32	11.0 ± 0.55	7 ± 1
Hammerhead	65r	41	3.4	0.18 ± 0.01	1.92	1.49 ± 0.82	>49
Hammerhead	67r	31	3.4	0.22 ± 0.02	2.37	0.70 ± 0.51	>98
Hammerhead	68r	59	3.4	0.18 ± 0.01	1.97	6.02 ± 0.56	5 ± 1
Hammerhead	70r	41	3.4	0.04 ± 0.01	0.43	0.00 ± 0.23	>39
Hammerhead	71r	45	3.4	0.11 ± 0.01	1.18	0.73 ± 0.52	>47
Hammerhead	87r	44	3.4	0.10 ± 0.01	1.13	1.23 ± 0.72	>32
Hammerhead	89r	41	3.4	0.07 ± 0.01	0.77	2.81 ± 0.46	3 ± 1
Hammerhead	90r	58	3.4	0.03 ± 0.01	0.35	0.74 ± 0.52	>14
Hammerhead	91r	55	3.4	0.15 ± 0.01	1.67	0.70 ± 0.51	>67
Q0055-269	3b	39	3.4	0.11 ± 0.01	1.18	0.13 ± 0.32	>75
Q0055-269	4b	46	3.5	0.15 ± 0.01	1.78	0.21 ± 0.40	>86
Q0055-269	5b	42	3.5	0.17 ± 0.01	1.96	-0.13 ± 0.19	>200
Q0055-269	1q	50	3.6	0.14 ± 0.01	1.66	-0.05 ± 0.19	>159
Q0055-269	2q	253	3.6	2.08 ± 0.05	25.6	1.67 ± 1.00	64 ± 38
Q0055-269	5q	63	3.6	0.57 ± 0.02	6.99	1.67 ± 0.54	91 ± 30
Q0055-269	7q	49	3.6	0.19 ± 0.01	2.34	0.30 ± 0.49	>84
Q0055-269	17q	118	3.6	0.61 ± 0.02	7.49	0.68 ± 0.65	58 ± 55
Q0055-269	19q	33	3.6	0.27 ± 0.02	3.39	0.38 ± 0.56	>105
Q0055-269	20q	45	3.6	0.26 ± 0.02	3.27	1.60 ± 0.37	14 ± 3
Q0055-269	31q	156	3.6	1.23 ± 0.04	15.5	1.66 ± 0.83	44 ± 22
Q0055-269	32q	52	3.7	0.58 ± 0.02	7.49	0.96 ± 0.27	119 ± 34
Q0055-269	38q	190	3.7	3.11 ± 0.06	40.3	2.78 ± 0.74	109 ± 29

Table 5
(Continued)

Field	ID	Area (pixels ²)	Redshift	Flux(Ly α) (10 ⁻¹⁷ erg s ⁻¹ cm ⁻²)	L(Ly α) (10 ⁴¹ erg s ⁻¹)	Flux(Cont _{PSF}) (10 ⁻²⁰ erg s ⁻¹ cm ⁻² Å ⁻¹)	EW ₀ (Ly α) (Å)
Q0055–269	1r	61	3.7	0.22 ± 0.02	3.02	0.17 ± 0.27	>171
Q0055–269	3r	33	3.8	0.07 ± 0.01	0.97	-0.09 ± 0.10	>143
Q0055–269	12r	42	3.8	0.27 ± 0.02	3.78	1.68 ± 0.36	59 ± 13
Q0055–269	14r	97	3.8	0.51 ± 0.02	7.33	0.72 ± 0.55	127 ± 96
Q1317–0507	1b	113	3.5	0.83 ± 0.03	9.36	1.24 ± 0.68	16 ± 9
Q1317–0507	3b	125	3.5	1.28 ± 0.04	14.7	0.90 ± 0.81	21 ± 19
Q1317–0507	9b	174	3.6	1.21 ± 0.03	14.8	1.01 ± 0.96	17 ± 16
Q1317–0507	12b	72	3.6	1.17 ± 0.03	14.4	1.14 ± 0.62	19 ± 10
Q1317–0507	18b	36	3.6	0.19 ± 0.01	2.37	0.07 ± 0.28	>147
Q1317–0507	3q	46	3.6	0.43 ± 0.02	5.53	4.88 ± 0.29	12 ± 1
Q1317–0507	4q	77	3.6	0.55 ± 0.02	7.08	0.66 ± 0.64	11 ± 11
Q1317–0507	7q	74	3.7	0.40 ± 0.02	5.26	1.82 ± 0.63	10 ± 3
Q1317–0507	3r	26	3.8	0.13 ± 0.01	1.85	-0.03 ± 0.21	>130
Q1317–0507	6r	44	3.8	0.10 ± 0.01	1.37	0.30 ± 0.51	>40
Q1317–0507	16r	99	3.9	1.12 ± 0.03	17.2	8.80 ± 0.56	17 ± 1
Q1317–0507	17r	51	3.9	0.09 ± 0.01	1.31	0.27 ± 0.48	>36
Q1621–0042	1b	38	3.5	0.23 ± 0.02	2.62	0.25 ± 0.52	>100
Q1621–0042	2b	30	3.5	0.24 ± 0.02	2.77	0.41 ± 0.68	>80
Q1621–0042	5b	33	3.5	0.24 ± 0.02	2.77	0.05 ± 0.32	>168
Q1621–0042	4b	149	3.5	1.41 ± 0.04	16.3	1.28 ± 1.12	37 ± 33
Q1621–0042	9b	28	3.6	0.26 ± 0.02	3.19	1.54 ± 0.42	18 ± 5
Q1621–0042	10b	50	3.6	0.21 ± 0.01	2.59	1.38 ± 0.65	14 ± 7
Q1621–0042	11b	43	3.6	0.17 ± 0.01	2.04	0.25 ± 0.52	>69
Q1621–0042	1q	41	3.6	0.11 ± 0.01	1.41	0.59 ± 0.86	>28
Q1621–0042	2r	42	3.8	0.02 ± 0.01	0.30	-0.23 ± 0.27	>16
Q1621–0042	3r	136	3.8	3.39 ± 0.06	48.2	0.45 ± 1.04	198 ± 460
Q1621–0042	7r	137	3.9	8.69 ± 0.09	130.0	0.45 ± 0.95	45 ± 97
Q1621–0042	9r	61	3.9	0.42 ± 0.02	6.41	0.47 ± 0.73	>117
Q1621–0042	10r	72	3.9	0.68 ± 0.03	10.4	0.57 ± 0.84	>165
Q1621–0042	11r	114	3.9	1.80 ± 0.04	27.6	6.72 ± 0.74	32 ± 4
Q2000–330	2b	45	3.5	0.06 ± 0.01	0.73	-0.05 ± 0.20	>68
Q2000–330	4b	36	3.5	0.24 ± 0.02	2.93	0.11 ± 0.32	>170
Q2000–330	5b	44	3.5	0.20 ± 0.01	2.46	0.27 ± 0.47	>94
Q2000–330	6b	47	3.5	0.40 ± 0.02	4.81	2.80 ± 0.37	97 ± 14
Q2000–330	7b	76	3.6	0.43 ± 0.02	5.21	1.23 ± 0.52	27 ± 11
Q2000–330	8b	47	3.6	0.21 ± 0.01	2.49	0.28 ± 0.48	>94
Q2000–330	14b	102	3.6	0.22 ± 0.02	2.75	0.37 ± 0.57	>84
Q2000–330	16b	87	3.6	0.54 ± 0.02	6.66	2.04 ± 0.57	74 ± 21
Q2000–330	25b	176	3.6	1.15 ± 0.03	14.5	0.77 ± 0.98	37 ± 46
Q2000–330	26b	48	3.6	0.30 ± 0.02	3.78	2.43 ± 0.41	12 ± 2
Q2000–330	27b	33	3.6	0.14 ± 0.01	1.80	0.26 ± 0.46	>67
Q2000–330	29b	65	3.6	0.29 ± 0.02	3.76	0.67 ± 0.61	11 ± 10
Q2000–330	1q	93	3.7	2.27 ± 0.05	30.6	1.54 ± 0.70	24 ± 11
Q2000–330	17q	42	3.8	0.47 ± 0.02	6.64	3.09 ± 0.30	5 ± 1
Q2000–330	19q	43	3.8	0.46 ± 0.02	6.45	0.65 ± 0.45	9 ± 6
Q2000–330	23q	38	3.8	0.17 ± 0.01	2.41	0.59 ± 0.79	>45
Q2000–330	1r	42	3.9	0.10 ± 0.01	1.49	-0.20 ± 0.20	>103
Q2000–330	5r ^a	59	3.9	0.72 ± 0.03	11.2	3.37 ± 0.29	10 ± 1
Q2000–330	8r	46	4.0	0.09 ± 0.01	1.44	-0.30 ± 0.20	>89

Note. The columns are (1) field, (2) object ID, (3) object area, (4) redshift, (5) Ly α flux, (6) Ly α luminosity, (7) continuum flux, (8) rest-frame equivalent width.

^a This particular target might also be classified as an [O II] emitter, although this alternative interpretation relies on the uncertain [O III] detection, which is hampered by telluric skylines.

(This table is available in machine-readable form.)

using Equation (8) in C12,

$$M_{\text{gas}} \sim 1.4 \times 10^9 M_{\odot} \left(\frac{L_{\text{Ly}\alpha}}{10^{42} \text{ erg s}^{-1}} \right) \left(\frac{T}{2 \times 10^4 \text{ K}} \right) C^{-1}, \quad (5)$$

we estimate gas masses spanning a range between $M_{\text{gas}} \sim 0.2$ and $6 \times 10^9 M_{\odot}$, similar to the DG candidates in C12.

To estimate their limit on the star formation rate (SFR), we use the limit on their continuum magnitude (28.8 AB mag extracted from a 1'' diameter aperture from the stacked continuum image—see Figure 13—re-centered at the position of the DG candidates) and convert this value into an SFR following Otf-Flornes & Mas-Hesse (2010) and assuming: (i) a Salpeter IMF, (ii) a color excess $E(B-V) = 0$, and (iii) an

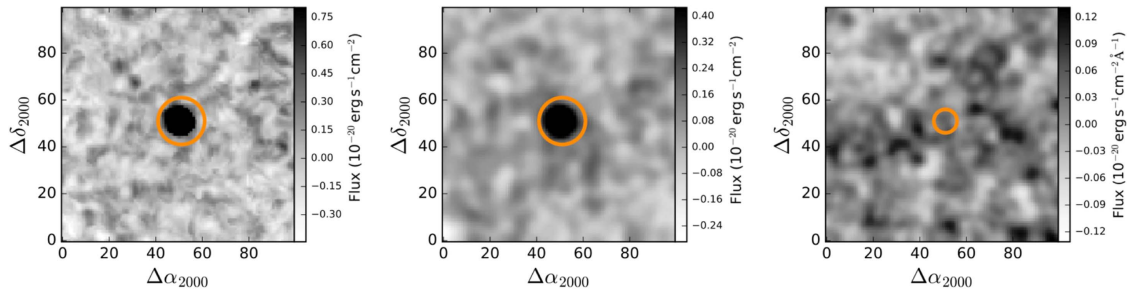


Figure 13. Postage images for the high- z DG candidates stacking. The optimally extracted image is shown in the first panel, while the classical pseudo-NB and the continuum images are shown in the second and third panels, respectively. The orange circles indicate the positions of the detected target at the center of the images.

extended burst of 250 Myr. The constraint achieved for the SFR is $0.02 M_{\odot} \text{ yr}^{-1}$, which yields a star formation efficiency SFE ($=\text{SFR}/M_{\text{gas}}$) of $2.13 \times 10^{-11} \text{ yr}^{-1}$, indicating that, similar to their analogues at $z \approx 2.4$ (C12), our DGs are very inefficient at forming stars.

Finally, the distribution of boosted fluorescent LAEs can also be used to constrain the QSO lifetimes (e.g., Cantalupo et al. 2007; Trainor & Steidel 2013; Borisova et al. 2016b). Assuming that our DG candidates are fluorescently illuminated by the QSO, we used the simple geometrical model presented in Borisova et al. (2016a) to constrain how long the QSO was shining on these protoclusters of neutral gas, i.e., the QSO lifetime t_Q . Considering the most distant DG candidate within our sample and taking the mean error in the systemic redshift into account, we obtain a distance of 8.7 physical Mpc, which corresponds to $t_Q \sim 60$ Myr. We note that our QSO lifetime calculation is based on MUSE observations that are more sensitive to more distant QSO-induced fluorescent Ly α emission. Our estimate is compatible with the results obtained for different QSOs at redshift ~ 3 analyzed in previous studies (see also Trainor & Steidel 2013; Borisova et al. 2016a).

6. Summary and Conclusions

We made use of medium-deep (~ 10 hr) MUSE IFU GTO observations around five bright QSOs and one Type II AGN in our search for fluorescently illuminated DGs at $z > 3.2$ among LAEs in the proximity of the quasars. Previous surveys based on NB imaging (e.g., C12) were restricted to a fixed volume. The distinct capabilities of the MUSE instrument allowed us to build control samples at large distances from the quasars making use of the same data, and the same data reduction and analysis techniques.

Within a volume of 90 physical Mpc^3 , including the control sample regions, we have identified ~ 200 line emitters using the automatic source extraction software CubExtractor (S. Cantalupo 2018, in preparation) complemented with visual analysis. After inspecting their spectral properties in the large wavelength range provided by MUSE, we found that 186 of these sources are LAEs between redshifts 3.1 and 4.0 (see Table 5). We estimated their $\text{EW}_0(\text{Ly}\alpha)$ in a homogeneous way among the main and the control samples using two different approaches depending on whether or not the sources are detected in the continuum. Among all LAEs, we found 11 objects with $\text{EW}_0(\text{Ly}\alpha)$ lower limits larger than 240 \AA , the theoretical limit for galaxies with a PopII stellar population (Charlot & Fall 1993; Malhotra & Rhoads 2002). The analysis of the $\text{EW}_0(\text{Ly}\alpha)$ distribution revealed that these high- EW_0 LAEs tend to preferentially reside within $\sim 10^4 \text{ km s}^{-1}$ from the quasar systemic redshift. In particular, six of the eight LAEs with $\text{EW}_0(\text{Ly}\alpha) > 240 \text{ \AA}$ in

our high-redshift sample lie in close proximity to the QSOs. These sources represent about 25% of all LAEs detected within a velocity distance of $\sim 10^4 \text{ km s}^{-1}$ from the high-redshift quasars in our sample. This fraction is significantly higher than the corresponding value in the control samples (4%).

This excess of high- EW_0 sources correlated with distance from the quasar is completely consistent with the expectations of quasar fluorescent illumination (e.g., Cantalupo et al. 2007; Trainor & Steidel 2012; Borisova et al. 2016b, C12). Alternative scenarios would require a tight link between distance from the quasars and intrinsic galaxy properties. However, the lack of any correlation between the number density of detected LAEs and their luminosities with the distance from the quasars (consistent with other surveys) does not support these alternative scenarios.




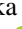

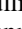
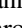









In the fluorescent case, the eight LAEs with $\text{EW}_0(\text{Ly}\alpha) > 240 \text{ \AA}$ and without the continuum counterpart located in the close proximity of the QSOs represent the best candidates so far for DGs at $z > 3$. Their properties, such as their number densities, compact morphology, luminosities, derived gas masses ($\sim 10^9 M_{\odot}$), and star formation efficiencies (SFEs $< 2.13 \times 10^{-11} \text{ yr}^{-1}$) are remarkably similar to their analogues detected at $z \approx 2.4$ with NB imaging by C12.

Although our current sample is limited, this study demonstrates the potential of MUSE observations for the robust detection and characterization of DG candidates fluorescently illuminated by quasars at $z > 3$. Compared to NB imaging, the main limitation given by the relatively small MUSE FoV is compensated by the large wavelength range (offering the opportunity to build robust control samples), the immediate spectroscopic confirmation, and the lack of filter (and slit) losses. Every QSO field observed with MUSE will therefore offer the potential to discover new DG candidates and provide crucial information on the early and dark phases of galaxy formation.

The authors thank the anonymous referee for the enlightening suggestions, which helped to improve the quality of this manuscript. This work is based on observations taken at ESO/VLT in Paranal, and we would like to thank the ESO staff for their assistance and support during the MUSE GTO campaigns. This work was supported by the Swiss National Science Foundation. We thank Amanda Bluck for proofreading the manuscript. We thank J. Woo and M. Maseda for their comments on the draft. S.C. gratefully acknowledges support from Swiss National Science Foundation grant PP00P2_163824. R.B. acknowledges support from the ERC advanced grant 339659-MUSICOS. J.R. acknowledges support from the ERC starting grant 336736-CALENDS. J.B. acknowledges support

by Fundação para a Ciência e a Tecnologia (FCT) through national funds (UID/FIS/04434/2013) and Investigador FCT contract IF/01654/2014/CP1215/CT0003., and by FEDER through COMPETE2020 (POCI-01-0145-FEDER-007672). T.C. acknowledges support of the ANR FOGHAR (ANR-13-BS05-0010-02), the OCEVU Labex (ANR-11-LABX-0060), and the A*MIDEX project (ANR-11-IDEX-0001-02) funded by the “Investissements d’avenir” French government program managed by the ANR. J.S. and S.M. acknowledge support from European Research Council (ERC), grant agreement 278594-GasAroundGalaxies. J.S. acknowledges support from the Netherlands Organisation for Scientific Research (NWO) VICI grant 639.043.409. This research made use of Astropy, a community-developed core Python package for astronomy (Astropy Collaboration et al. 2013), NumPy and SciPy (Oliphant 2007), Matplotlib (Hunter 2007), IPython (Perez & Granger 2007), and of NASA’s Astrophysics Data System Bibliographic Services.

ORCID iDs

Raffaella Anna Marino  <https://orcid.org/0000-0002-8559-6565>
 Simon J. Lilly  <https://orcid.org/0000-0002-6423-3597>
 Sofia G. Gallego  <https://orcid.org/0000-0002-8825-8107>
 Lorrie A. Straka  <https://orcid.org/0000-0001-5892-6760>
 Elena Borisova  <https://orcid.org/0000-0002-1794-3596>
 Gabriele Pezzulli  <https://orcid.org/0000-0003-0736-7879>
 Jarle Brinchmann  <https://orcid.org/0000-0003-4359-8797>
 C. Marcella Carollo  <https://orcid.org/0000-0003-1624-7609>
 Joseph Caruana  <https://orcid.org/0000-0002-6089-0768>
 Simon Conseil  <https://orcid.org/0000-0002-3657-4191>
 Thierry Contini  <https://orcid.org/0000-0003-0275-938X>
 Hayley Finley  <https://orcid.org/0000-0002-1216-8914>
 Sowgat Muzahid  <https://orcid.org/0000-0003-3938-8762>
 Johan Richard  <https://orcid.org/0000-0001-5492-1049>
 Joop Schaye  <https://orcid.org/0000-0002-0668-5560>
 Martin Wendt  <https://orcid.org/0000-0001-5020-9994>

References

- Astropy Collaboration, Robitaille, T. P., Tollerud, E. J., et al. 2013, *A&A*, 558, A33
- Bacon, R., Accardo, M., Adjali, L., et al. 2010, *Proc. SPIE*, 7735, 773508
- Bacon, R., Brinchmann, J., Richard, J., et al. 2015, *A&A*, 575, A75
- Bertin, E., & Arnouts, S. 1996, *A&AS*, 117, 393
- Boera, E., Murphy, M. T., Becker, G. D., et al. 2014, *MNRAS*, 441, 1916
- Borisova, E. 2016, PhD Dissertation, ETH Zürich, 23603
- Borisova, E., Cantalupo, S., Lilly, S. J., et al. 2016a, *ApJ*, 831, 39
- Borisova, E., Lilly, S. J., Cantalupo, S., et al. 2016b, *ApJ*, 830, 120
- Calverley, A. P., Becker, G. D., Haehnelt, M. G., & Bolton, J. S. 2011, *MNRAS*, 412, 2543
- Cantalupo, S. 2010, *MNRAS*, 403, L16
- Cantalupo, S. 2017, *ASSL*, 430, 195
- Cantalupo, S., Arrigoni-Battaia, F., Prochaska, J. X., Hennawi, J. F., & Madau, P. 2014, *Natur*, 506, 63
- Cantalupo, S., Lilly, S. J., & Haehnelt, M. G. 2012, *MNRAS*, 425, 1992
- Cantalupo, S., Lilly, S. J., & Porciani, C. 2007, *ApJ*, 657, 135
- Cantalupo, S., Porciani, C., Lilly, S. J., & Miniati, F. 2005, *ApJ*, 628, 61
- Capak, P. L., Teplitz, H., Hanish, D., et al. 2012, in AAS Meeting, 219, 410
- Carswell, R. F., Whelan, J. A. J., Smith, M. G., Boksenberg, A., & Tytler, D. 1982, *MNRAS*, 198, 91
- Charlot, S., & Fall, S. M. 1993, *ApJ*, 415, 580
- Cimatti, A., Mignoli, M., Daddi, E., et al. 2002, *A&A*, 392, 395
- Cooksey, K. L., Kao, M. M., Simcoe, R. A., et al. 2013, *ApJ*, 763, 37
- Dall’Aglia, A., Wisotzki, L., & Worseck, G. 2008, *A&A*, 491, 465
- Dekel, A., Birnboim, Y., Engel, G., et al. 2009, *Natur*, 457, 451
- Drake, A. B., Guiderdoni, B., Blaizot, J., et al. 2017, *MNRAS*, 471, 267
- Feldman, G. J., & Cousins, R. D. 1998, *PhRvD*, 57, 3873
- Francis, P. J., & Bland-Hawthorn, J. 2004, *MNRAS*, 353, 301
- Fumagalli, M., Cantalupo, S., Dekel, A., et al. 2016, *MNRAS*, 462, 1978
- Fumagalli, M., Haardt, F., Theuns, T., et al. 2017, *MNRAS*, 467, 4802
- Fumagalli, M., Hennawi, J. F., Prochaska, J. X., et al. 2014, *ApJ*, 780, 74
- Fumagalli, M., O’Meara, J. M., & Prochaska, J. X. 2011, *Sci*, 334, 1245
- Fynbo, J. P. U., Ledoux, C., Møller, P., Thomsen, B., & Burud, I. 2003, *A&A*, 407, 147
- Gavazzi, G., Giovanelli, R., Haynes, M. P., et al. 2008, *A&A*, 482, 43
- Giavalisco, M., Vanzella, E., Salimbeni, S., et al. 2011, *ApJ*, 743, 95
- Giovanelli, R., Haynes, M. P., Kent, B. R., et al. 2005, *AJ*, 130, 2598
- Gould, A., & Weinberg, D. H. 1996, *ApJ*, 468, 462
- Haiman, Z., & Rees, M. J. 2001, *ApJ*, 556, 87
- Hashimoto, T., Garel, T., Guideroni, B., et al. 2017, *A&A*, 608, 10
- Hennawi, J. F., & Prochaska, J. X. 2013, *ApJ*, 766, 58
- Hinshaw, G., Larson, D., Komatsu, E., et al. 2013, *ApJS*, 208, 19
- Hogan, C. J., & Weymann, R. J. 1987, *MNRAS*, 225, 1P
- Hunter, J. D. 2007, *CSE*, 55
- Johnson, S. D., Chen, H.-W., & Mulchaey, J. S. 2015, *MNRAS*, 452, 2553
- Kikuta, S., Imanishi, M., Matsuoka, Y., et al. 2017, *ApJ*, 841, 128
- Kollmeier, J. A., Zheng, Z., Davé, R., et al. 2010, *ApJ*, 708, 1048
- Krumholz, M. R., & Dekel, A. 2012, *ApJ*, 753, 16
- Kuhlen, M., Krumholz, M. R., Madau, P., Smith, B. D., & Wise, J. 2012, *ApJ*, 749, 36
- Kuhlen, M., Madau, P., & Krumholz, M. R. 2012, *ApJ*, 776, 34
- Lau, M. W., Prochaska, J. X., & Hennawi, J. F. 2016, *ApJS*, 226, 25
- Leclercq, F., Bacon, R., Wisotzki, L., et al. 2017, *A&A*, 608, 8
- Lee, K.-G., Hennawi, J. F., Stark, C., et al. 2014, *ApJL*, 795, L12
- Lusso, E., Worseck, G., Hennawi, J. F., et al. 2015, *MNRAS*, 449, 4204
- Malhotra, S., & Rhoads, J. E. 2002, *ApJL*, 565, L71
- Martin, N. F., Ibata, R. A., Rich, R. M., et al. 2014, *ApJ*, 786, 106
- Meiksin, A. A. 2009, *RvMP*, 81, 1405
- Meurer, G. R., Heckman, T. M., & Calzetti, D. 1999, *ApJ*, 521, 64
- North, P. L., Marino, R. A., Gorgoni, C., et al. 2017, *A&A*, 604, 23
- Oke, J. B., & Gunn, J. E. 1983, *ApJ*, 266, 713
- Oliphant, T. E. 2007, *CSE*, 58
- O’Meara, J. M., Lehner, N., Howk, J. C., et al. 2015, *AJ*, 150, 111
- Orsi, A., Lacey, C. G., & Baugh, C. M. 2012, *MNRAS*, 425, 87
- Oti-Floranes, H., & Mas-Hesse, J. M. 2010, *A&A*, 511, A61
- Pâris, I., Petitjean, P., Aubourg, É., et al. 2012, *A&A*, 548, A66
- Pérez, F., & Granger, B. E. 2007, *CSE*, 53
- Prochaska, J. X., Hennawi, J. F., Lee, K.-G., et al. 2013a, *ApJ*, 776, 136
- Prochaska, J. X., Hennawi, J. F., & Simcoe, R. A. 2013b, *ApJL*, 762, L19
- Raiter, A., Schaerer, D., & Fosbury, R. A. E. 2010, *A&A*, 523, A64
- Rauch, M., Haehnelt, M., Bunker, A., et al. 2008, *ApJ*, 681, 856
- Rudie, G. C., Steidel, C. C., Trainor, R. F., et al. 2012, *ApJ*, 750, 67
- Schaerer, D. 2002, *A&A*, 382, 28
- Schaerer, D. 2003, *A&A*, 397, 527
- Schaye, J., Aguirre, A., Kim, T.-S., et al. 2003, *ApJ*, 596, 768
- Schmidt, M., Schneider, D. P., & Gunn, J. E. 1987, *ApJL*, 316, L1
- Schneider, D. P., Richards, G. T., Hall, P. B., et al. 2010, *AJ*, 139, 2360
- Seibert, M., Wyder, T., Neill, J., et al. 2012, in AAS Meeting, 219, 340
- Shapiro, L. G., & Stockman, G. C. 2001, Computer Vision (Upper Saddle River, NJ: Prentice-Hall)
- Shen, Y., Brandt, W. N., Richards, G. T., et al. 2016, *ApJ*, 831, 7
- Shibuya, T., Ouchi, M., Nakajima, K., et al. 2014, *ApJ*, 785, 64
- Swinbank, A. M., Vernet, J. D. R., Smail, I., et al. 2015, *MNRAS*, 449, 1298
- Tolman, R. C. 1930, *PNAS*, 16, 511
- Tolman, R. C. 1934, Relativity, Thermodynamics, and Cosmology (Oxford: Clarendon Press)
- Trainor, R. F., & Steidel, C. C. 2012, *ApJ*, 752, 39
- Trainor, R. F., & Steidel, C. C. 2013, *ApJL*, 775, L3
- Turner, M. L., Schaye, J., Steidel, C. C., et al. 2014, *MNRAS*, 445, 794
- Uchiyama, H., Toshikawa, J., Kashikawa, N., et al. 2018, *PASJ*, 70, S32
- Véron-Cetty, M. P., & Véron, P. 2010, *A&A*, 518, A10
- Vogt, S. S., Allen, S. L., Bigelow, B. C., et al. 1994, *Proc. SPIE*, 2198, 362
- Weilbacher, P. M. 2015, Science Operations 2015: Science Data Management, Zenodo, doi:10.5281/zenodo.3465
- Wisotzki, L., Bacon, R., Blaizot, J., et al. 2016, *A&A*, 587, A98
- York, D. G., Adelman, J., Anderson, J. E., Jr., et al. 2000, *AJ*, 120, 1579
- Zafar, T., Péroux, C., Popping, A., et al. 2013, *A&A*, 556, A141